An unrecognized inertial force induced by flow curvature in microfluidics

Siddhansh Agarwal^{a,1}, Fan Kiat Chan^{a,1}, Bhargav Rallabandi^b, Mattia Gazzola^{a,c,d,2}, and Sascha Hilgenfeldt^{a,2}

^aDepartment of Mechanical Science and Engineering, University of Illinois at Urbana–Champaign, Urbana, IL 61801; ^bDepartment of Mechanical Engineering, University of California, Riverside, CA 92521; National Center for Supercomputing Applications, University of Illinois at Urbana-Champaign, Urbana, IL 61801; and dCarl R. Woese Institute for Genomic Biology, University of Illinois at Urbana–Champaign, Urbana, IL 61801

Edited by David A. Weitz, Harvard University, Cambridge, MA, and approved May 23, 2021 (received for review February 25, 2021)

Modern inertial microfluidics routinely employs oscillatory flows around localized solid features or microbubbles for controlled, specific manipulation of particles, droplets, and cells. It is shown that theories of inertial effects that have been state of the art for decades miss major contributions and strongly underestimate forces on small suspended objects in a range of practically relevant conditions. An analytical approach is presented that derives a complete set of inertial forces and quantifies them in closed form as easy-to-use equations of motion, spanning the entire range from viscous to inviscid flows. The theory predicts additional attractive contributions toward oscillating boundaries, even for density-matched particles, a previously unexplained experimental observation. The accuracy of the theory is demonstrated against full-scale, three-dimensional direct numerical simulations throughout its range.

inertial microfluidics | oscillatory flows | particle manipulation

D escribing effects of small, but finite, inertia on suspended particles is a fundamental fluid-dynamical problem that has never been solved in full generality (1-6). Modern microfluidics has turned this academic problem into a practical challenge through the use of high-frequency ($\omega \sim$ kilohertz to megahertz) oscillatory flows, perhaps the most efficient way to take advantage of inertial effects at low Reynolds numbers, to precisely manipulate particles, cells, and vesicles without the need for charges or chemistry (7-9). The systematic theoretical understanding of flow forces on particles has so far hinged on the pioneering work of Maxey and Riley (MR) (10), introduced almost 40 years ago and encompassing a number of specialized approaches (11–13), including acoustic secondary radiation forces (SRFs) that have been invoked to rationalize observed attractive forces toward localized features in oscillatory flows (8, 14–17). However, recent experimental (18) and theoretical (19) advances have shown that the classical MR theory falls significantly short of explaining the magnitude of attraction. We demonstrate here theoretically and computationally that previously unrecognized, significant forces act toward oscillating boundaries, even on neutrally buoyant particles, stemming from the interplay of particle inertia, flow gradients, and flow curvature. These forces cannot be understood quantitatively or qualitatively by MR (or SRF) and, instead, naturally emerge from a systematic generalization of MR, paving the way for enhanced and novel inertial microfluidic applications of great potential benefit in biomanufacturing, health, and medicine.

Oscillatory microfluidics is usually set up by or past a localized object [e.g., a microbubble or a no-slip solid (8, 20)], resulting in spatially nonuniform flows characterized by strong variations on gradient L_{Γ} and curvature L_{κ} length scales. Such flows exert remarkably consistent and controllable forces on particles and have been employed with great success for guidance, separation, aggregation, and sorting (9, 14, 21-25). Nonetheless, it is precisely this use of localized oscillations in modern microfluidics that is now pushing the envelope of the MR equation, exposing

its limits in predicting the emergence and magnitude of observed significant and persistent forces. Here, we provide a thorough revision of its theoretical foundations, but first, in light of the importance of this work for applications, we state a major practical outcome: In any oscillatory background flow field \bar{U} associated with a localized object, a density-matched (ρ) spherical particle of radius a_n experiences an attractive force toward the object. The component of this force along the object-to-particle connector e takes the explicit form

$$F_{\Gamma\kappa} = m_f \left\langle a_p^2 \nabla \bar{\boldsymbol{U}} : \nabla \nabla \bar{\boldsymbol{U}} \right\rangle \mathcal{F}(\lambda) \cdot \boldsymbol{e},$$
 [1]

where $m_f = 4\pi \rho a_p^3/3$ is the displaced fluid mass and the inner product represents the interaction of flow gradients and curvatures. Force [1] is steady, resulting from a time average $\langle \cdot \rangle$. The effect of oscillation frequency is quantified by the universal, analytically derived function \mathcal{F} of the Stokes number λ . For harmonic oscillatory flows, $\lambda \equiv a_v^2 \omega/(3\nu)$ and to excellent approximation $\mathcal{F}(\lambda)$ reads

$$\mathcal{F}(\lambda) = \frac{1}{3} + \frac{9}{16} \sqrt{\frac{3}{2\lambda}},$$
 [2]

valid over the entire range from the viscous $\lambda \ll 1$ to the inviscid $\lambda \gg 1$ limits. In practice, [1] moves a particle against its Stokes mobility along a radial coordinate measuring distance r_p from the localized object, so that the steady equation of motion becomes simply

Significance

Through a combination of theory and high-resolution simulations, we derive, isolate, and understand a previously unrecognized, strong force acting on particles in inertial microfluidic settings. The analysis applies especially to particle manipulation in fast oscillatory flows, a major tool in lab-on-a-chip processing as well as in diagnostic and biomanufacturing applications. Our approach systematically extends the Maxey-Riley equation, the main theoretical foundation for quantifying fluid forces on particles, to account for unexplained observations related to localized flow curvature and irreversible motion at low Reynolds

Author contributions: S.A., F.K.C., B.R., M.G., and S.H. designed research; S.A. and F.K.C. performed research; S.A. and F.K.C. analyzed data; and S.A., F.K.C., B.R., M.G., and S.H. wrote the paper.

The authors declare no competing interest.

This article is a PNAS Direct Submission.

Published under the PNAS license.

This article contains supporting information online at https://www.pnas.org/lookup/suppl/ doi:10.1073/pnas.2103822118/-/DCSupplemental.

Published July 14, 2021.

¹S.A. and F.K.C. contributed equally to this work.

²To whom correspondence may be addressed. Email: sascha@illinois.edu or mgazzola@illinois.edu.

$$\frac{dr_p}{dt} = \frac{F_{\Gamma\kappa}}{6\pi a_p \nu \rho},\tag{3}$$

with ν the kinematic viscosity of the fluid. For generic flows, $F_{\Gamma\kappa} < 0$, since the amplitude of \bar{U} decays with distance from the oscillating object, indicating attraction. If an additional steady-flow component is present, Eq. 3 quantifies the deviation between particle and fluid motion.

The above equations completely describe the particle dynamics and stem from a rigorous, general formalism developed below to respond to discrepancies observed experimentally. Indeed, as illustrated in Fig. 1 A and B, when neutrally buoyant particles of moderate λ approach the surface of oscillating bubbles (cf. refs. 9, 24, 32, and 33), we find evidence of significant radial attractive forces, even at a considerable distance from the bubble. This observation is in direct contradiction to existing theories such as SRF (8, 14, 16, 18, 19, 22, 23, 26–31), which either predict no attraction at all or a much too weak effect (see legend of Fig. 1 and *SI Appendix* for more details).

Our goal here is to develop a unifying theory that explains observations, accounts for particle inertia, and seamlessly spans the full viscous-to-inviscid operational flow spectrum. Accordingly, we revisit MR (10) and systematically account for all leading-order terms in particle Reynolds number $Re_p =$ $a_p U^*/\nu$, with U^* the velocity scale of the background flow. We then reveal their effect through a specially constructed case: a bubble of radius a_b oscillating in pure volume (breathing) mode, with a spherical, neutrally buoyant particle placed at an initial center-to-center distance $r_p(0)$. This scenario induces no rectified (streaming) flow in the absence of the particle (34) and, therefore, allows for the precise evaluation of the newly considered disturbance flow effects introduced by the particle itself. The analysis is complemented by direct numerical simulations (DNSs) that provide first-principle solutions of flow field and particle displacement. Fig. 1 C, Upper shows that the computed oscillatory-flow component closely resembles the background flow, even in the presence of the particle, while time-averaging over an oscillation cycle (Fig. 1 C, Lower) reveals the much richer secondary steady disturbance flow induced by the particle.

Like MR, we wish to describe the hydrodynamic forces on a particle centered at r_p using only information from the given undisturbed background flow \bar{U} . We fix a (moving) coordinate system at r_p and nondimensionalize lengths

by a_p , times by ω^{-1} , and velocities by U^* (using lower-case letters for nondimensional velocities). A spherical particle exposed to a known (laboratory-frame) background flow \bar{u} and moving with velocity u_p (neglecting effects of rotation) then experiences the effects of the undisturbed flow $\mathbf{w}^{(0)} = \bar{\mathbf{u}} - \mathbf{u}_p$ and a disturbance flow $\mathbf{w}^{(1)}$. Following ref. 10, the latter obeys

$$\nabla^{2} \mathbf{w}^{(1)} - \nabla p^{(1)} = 3\lambda \frac{\partial \mathbf{w}^{(1)}}{\partial t} + \text{Re}_{R} \mathbf{f}, \quad \text{where}$$

$$\mathbf{f} = \mathbf{w}^{(0)} \cdot \nabla \mathbf{w}^{(1)} + \mathbf{w}^{(1)} \cdot \nabla \mathbf{w}^{(0)} + \mathbf{w}^{(1)} \cdot \nabla \mathbf{w}^{(1)},$$
[4]

with boundary conditions $\mathbf{w}^{(1)} = \mathbf{u}_p - \bar{\mathbf{u}}$ on r = 1, and $\mathbf{w}^{(1)} = 0$ as $r \to \infty$.

This equation is exact and does not rely on small Re_p . To obtain explicit results, we use two expansions: One, like MR, expands the background flow around the particle position into spatial moments of alternating symmetry:

$$\bar{u} = \bar{u}|_{r_p} + r \cdot E + rr : G + \dots,$$
 [5]

where $E = (a_p/L_{\Gamma})\nabla \bar{\boldsymbol{u}}|_{r_p}$ and $G = \frac{1}{2}(a_p^2/L_{\kappa}^2)\nabla\nabla \bar{\boldsymbol{u}}|_{r_p}$ capture the background-flow shear gradients and curvatures, whose scales are, in practice, much larger than a_p , justifying [5].

The other cornerstone of our theory is a regular perturbation expansion of all variables in [4], using subscripts for orders of Re_p , e.g., $\mathbf{w}^{(1)} = \mathbf{w}_0^{(1)} + \operatorname{Re}_p \mathbf{w}_1^{(1)} + \mathcal{O}(\operatorname{Re}_p^2)$. In contrast to MR, this retains a term $\operatorname{Re}_p f_0$ in [4], where $f_0 = \mathbf{w}^{(0)} \cdot \nabla \mathbf{w}_0^{(1)} + \mathbf{w}_0^{(1)} \cdot \nabla \mathbf{w}_0^{(1)} + \mathbf{w}_0^{(1)} \cdot \nabla \mathbf{w}_0^{(1)} + \mathbf{w}_0^{(1)} \cdot \nabla \mathbf{w}_0^{(1)}$ is the leading-order nonlinear forcing of the disturbance flow. Note also that $w_0^{(1)}$ is purely oscillatory, while $w_1^{(1)}$ has a nonzero time-average, exemplified by the flow in Fig. 1 C, Lower.

Forces on the particle, as integrals of the fluid stress tensor over the particle surface S_p are also expanded in this fashion. Application of a reciprocal theorem (cf. ref. 2) formally yields the inertial force components as volume integrals over the entire fluid domain without the need to explicitly compute the flow field at that order. The reciprocal theorem employs a known test

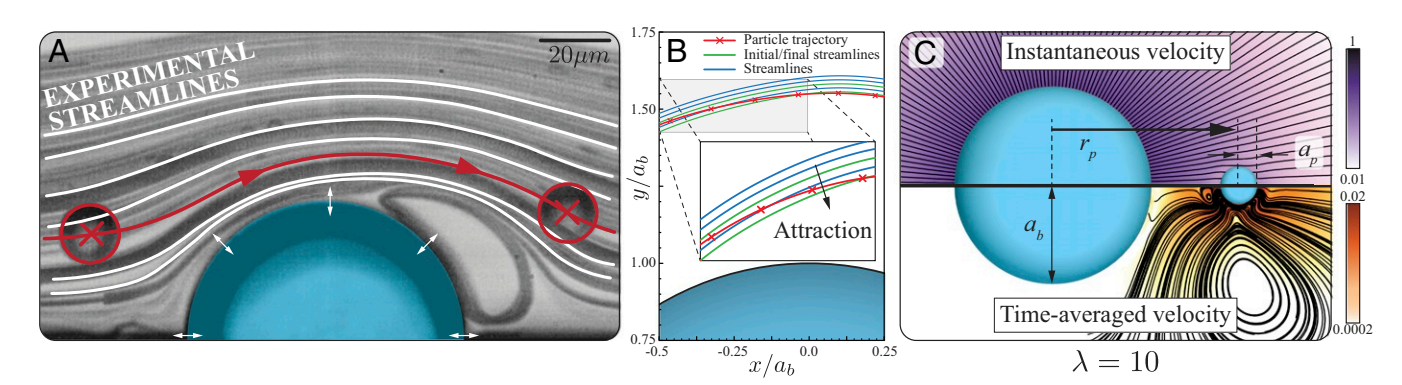


Fig. 1. Particle attraction to oscillating bubbles. (A) A polystyrene particle ($a_p = 10\mu m$, $\lambda \approx 4$) is transported past an oscillating microbubble ($a_b = 40\mu m$, $\omega/(2\pi) = 20$ kHz). (B) Close-up of the experimental trajectory (red) of a neutrally buoyant particle intersecting streamlines (blue), indicating a net attraction toward the bubble over fast time scales of a few milliseconds, unexplained by existing theories: Inertial particle migration due to shear gradients (4, 26, 27) is far slower; the SRF of acoustofluidics (22, 28–31) is proportional to the particle–fluid density contrast and thus vanishes here; an ad hoc theory for nearly invisció flows ($\lambda \gg 1$) from ref. 19 predicts an attraction much too weak to explain observations. A detailed discussion of this particular experiment in the context of our analysis is provided in SI Appendix. (C) Simulation of the prototypical problem: a particle exposed to the flow of a bubble oscillating in volume mode at relative amplitude ϵ . (C, Upper) Instantaneous streamlines (color bar is flow speed in units of U^*). (C, Lower) Time-averaged streamlines (color bar is steady-flow speed in units of ϵU^*).

flow u' = u'(t)e in a chosen direction e. The component of the equation of particle motion in that direction, to $\mathcal{O}(\text{Re}_p)$, is then

$$m_p \frac{dU_p}{dt} = F_0^{(0)} + F_0^{(1)} + \text{Re}_p(F_1^{(0)} + F_1^{(1)}) + \mathcal{O}(\text{Re}_p^2),$$
 [6a]

$$F_0^{(0)} = \frac{F_S}{6\pi} \int_V (3\lambda \partial_t \bar{\boldsymbol{u}}) \cdot \boldsymbol{e} dV,$$
 [6b]

$$F_0^{(1)} = \frac{F_S}{6\pi} \mathcal{L}^{-1} \left\{ \int_{S_p} \frac{\left(\hat{\boldsymbol{u}}_p - \hat{\boldsymbol{u}} \right)}{\hat{\boldsymbol{u}}'} \cdot (\hat{\boldsymbol{\sigma}}' \cdot \boldsymbol{n}) dS \right\}, \tag{6c}$$

$$F_1^{(0)} = \frac{F_S}{6\pi} \int_V (\bar{\boldsymbol{u}} \cdot \nabla \bar{\boldsymbol{u}}) \cdot \boldsymbol{e} \, dV, \qquad [6d]$$

$$F_{1}^{(1)} = -\frac{F_{S}}{6\pi} \mathcal{L}^{-1} \left\{ \frac{1}{\hat{u}'} \int_{V} \hat{\boldsymbol{u}}' \cdot \hat{\boldsymbol{f}}_{0} dV \right\}, \tag{6e}$$

where σ' is the stress tensor of the test flow, hats denote Laplace transforms, and \mathcal{L}^{-1} their inverse. All dimensional forces have the common Stokes drag scale $F_S/6\pi = \nu \rho a_p U^*$.

Eqs. 6b and 6d are forces exerted by the background flow, while Eqs. **6c** and **6e** stem from the disturbance flow. The original MR equation contains $F_0^{(0)}$ and $F_0^{(1)}$, but only part of $F_1^{(0)}$, while the particle inertia force $F_1^{(1)}$ has not been described previously. We shall show that these unrecognized contributions are not small corrections, but are dominant in relevant applications, particularly the inertial disturbance force $F_1^{(1)}$.

The outlined formalism is entirely general for arbitrary background flows and provides analytical expressions for the forces $F_1^{(0)}$ and $F_1^{(1)}$. The former straightforwardly reads

$$\frac{F_1^{(0)}}{F_S} = \frac{4}{9} (\mathbf{E} : \mathbf{G}) \cdot \mathbf{e} \, \mathcal{F}_1^{(0)},$$
 [7]

where $\mathcal{F}_1^{(0)}=1/5$ (35). The force $F_1^{(1)}$, by contrast, is generally composed of various contributions involving the expansion coefficients of Eq. 5; cf. Materials and Methods and SI Appendix. However, it simplifies greatly in oscillatory background flows that are potential: This condition is fulfilled in almost all cases, requiring only that the distance h_p between the particle and object surfaces is greater than the Stokes boundary-layer thickness $\delta_S = \sqrt{2\nu/\omega}$, which simplifies to the easily satisfied condition $\lambda \gtrsim (a_p/h_p)^2$. Then, the only way to construct a force vector from a contraction of the higher-rank tensors E and G is E: G (cf. refs. 36 and 37). If, furthermore, the particle is neutrally buoyant, the slip velocity u_s vanishes, and we obtain

$$\frac{F_1^{(1)}}{F_S} = \frac{4}{9} (E : G) \cdot e \, \mathcal{F}_1^{(1)}(\lambda), \tag{8}$$

where the function $\mathcal{F}_1^{(1)}(\lambda)$ is determined analytically (see *SI Appendix* for details) and is universal, i.e., valid for arbitrary flow fields. While both Eqs. 7 and 8 need nonzero gradient and curvature terms of the background flow, $\mathcal{F}_1^{(1)}(\lambda)$ captures the nonlinear effect of inertia of the leading-order unsteady disturbance flow $\mathbf{w}_0^{(1)}$ on the particle. For micrometer-size particles, where $\lambda \sim 1$, $\mathcal{F}_1^{(1)}$ is considerably larger than $\mathcal{F}_1^{(0)}$, so that Eq. 8 is the dominant effect in practical microfluidic applications. The sum of both contributions Eqs. 7 and 8 results in the dimensional force Eq. 1, before time-averaging.

We now turn to the prototypical oscillatory flow example of Fig. 1C. This flow field's unique scale is the bubble radius (L_{Γ} = $L_{\kappa} = a_b$). With an oscillation amplitude of ϵa_b ($\epsilon \ll 1$ in practical situations), the velocity scale is $U^* = \epsilon a_b \omega$, and we anticipate the relevant rectified (time-averaged) force to lead to irreversible particle motion proportional to ϵ^2 (cf. ref. 19). It is advantageous to change the length scale to a_b here, introducing $\alpha \equiv a_p/a_b$, and to change the coordinate origin to the bubble center, so that the background flow has only one component $\bar{u} = \sin t/r^2$ in the direction $e = e_T$. The oscillatory forces and the particle motion now follow explicitly (Materials and Methods).

Our ultimate goal is to predict the rectified trajectory of the particle after time-averaging over the fast oscillatory time scale, to provide practically useful guidance for precision applications. Time-scale separation using the slow time $T = e^2 t$ analogous to ref. 19 (Materials and Methods) obtains the leading-order equation for the rectified particle motion $r_p(T)$

$$\frac{dr_p}{dT} = -\frac{6}{r_p^7} \alpha^2 \lambda \mathcal{F}(\lambda),$$
 [9]

where $\mathcal{F}(\lambda) = \mathcal{F}_1^{(1)}(\lambda) + \mathcal{F}_1^{(0)}$. Eq. **9** is readily solved analytically and is analogous to the result Eq. **3**. Indeed, while the analytical form of the universal function $\mathcal{F}_1^{(1)}$ is complicated (*SI Appendix*), one can Taylor expand in both the viscous limit $(\lambda \to 0)$ and the inviscid limit $(\lambda \to \infty)$ to obtain

$$\mathcal{F}^{v} = \frac{9}{16}\sqrt{\frac{3}{2\lambda}} + \mathcal{O}(1), \quad \mathcal{F}^{i} = \frac{1}{3} + \mathcal{O}(1/\sqrt{\lambda}).$$
 [10]

The simple sum of these leading terms yields the uniformly valid expression [2] for the total dimensionless force $\mathcal{F}(\lambda)$ on the particle. Note that our derivation is based fundamentally on the presence of both viscous and inertial effects, so that even \mathcal{F}^v is a finite-inertia force. Its $\lambda^{-1/2}$ scaling for small λ is reminiscent of Saffman's lift force (38), but is obtained without decomposing the domain into viscous and inertial regions (Materials and *Methods*). Remarkably, the opposite limit \mathcal{F}^i exactly asymptotes to the result obtained from the purely inviscid formalism of ref. 19 as $\lambda \to \infty$.

We now demonstrate that Eq. 2 is accurate over the entire range of Stokes numbers by comparing our theory with independent, large-scale, three-dimensional (3D) numerical simulations, previously validated in a variety of streaming scenarios (39, 40). Fig. 2 A-E illustrate the rich time-averaged flow $\langle w \rangle$ at different λ , while Fig. 2 G and I exemplify the expected confinement of vorticity around the particle. The simulations also serve to justify our omission of an inertia-dominated outer region (Fig. 2 F and H). In Fig. 3A, we compare analytical and simulated particle trajectories on both the oscillatory and slow time scales. The classical MR equation fails to capture any of the attraction observed in DNS, while the present theory is in excellent agreement both for the instantaneous motion and the rectified drift of the particle. Moreover, it succeeds over the entire range of λ values; cf. Fig. 3 B–E. In the figure, we also see that the inviscid formalism of ref. 19 (dashed lines) gives a much too weak attraction, particularly for practically relevant $\lambda \sim 1$. This is an intuitive outcome of taking viscosity into account, as the Stokes boundary layer (cf. Fig. 2 G and I) effectively increases particle size, so that forces scaling with particle size (cf. Eq. 1) become larger. Fig. 3 also illustrates the great benefit of the analytical theory Eq. 9, as individual DNSs incur large computational costs of up to $\sim 100,000$ core-hours on the Stampede2 supercomputer (SI Appendix).

Fig. 4 summarizes the comparison between theory and simulations: Time-averaged DNS trajectories (beyond an initial

Downloaded at UNIV OF CALIFORNIA RIVERSIDE on July 14, 202



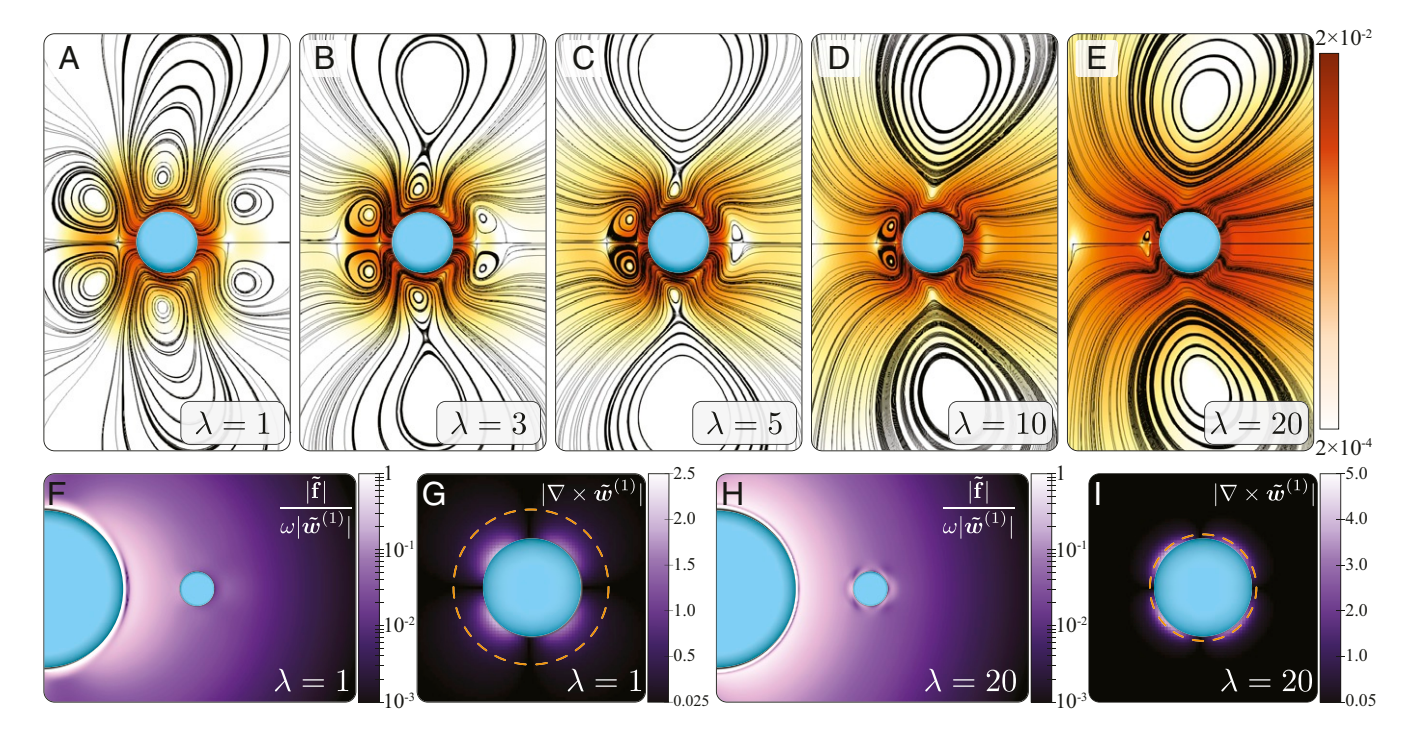


Fig. 2. Flow-field simulation results. (A–E) Streamlines of the steady flow $\langle w \rangle = \langle w^{(1)} \rangle$ (Stokes streamfunction isolines) for different λ ; color bar is velocity magnitude in units of ϵU^* . (F and H) The magnitude of Fourier-transformed quantities (indicated by tildes) evaluated at the driving frequency ω demonstrates that the flow field has no outer, inertia-dominated region. The ratio between oscillatory disturbance flow advective force $\tilde{\mathbf{f}}(\omega)$ and the Fourier component of the unsteady inertia $\partial w^{(1)}/\partial t$ remains small away from the bubble. (G and I) The Fourier component of vorticity at ω is confined to the oscillatory Stokes layer thickness δ_5 (orange-dashed circle) around the particle.

transient—see *SI Appendix* for details) for different values of λ were fitted to [9] to determine the dimensionless force \mathcal{F} . Our analytical predictions are in quantitative agreement with DNS across the range of λ , exhibiting an average error of $\approx 7\%$. This remaining discrepancy is attributed to effects of the narrowing distance between particle and bubble interface, which modifies the integration volume in Eq. **6e** and also compromises

the assumption of purely radial flow at the bubble interface, due to the particle disturbance flow.

Discussion

The data presented above demonstrate that particle motion can be described quantitatively by the forcing terms of Eqs. 7 and 8. It is furthermore important to show that other hydrodynamic force

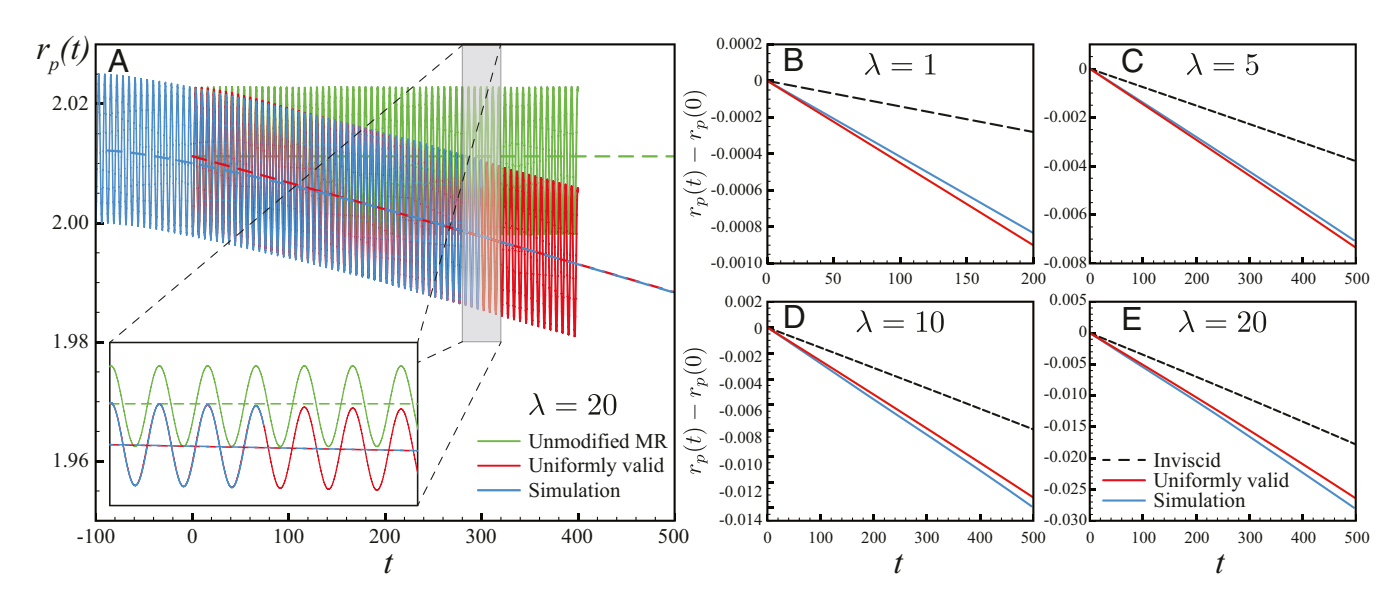


Fig. 3. Comparison of theoretical (red) and simulated (blue) particle dynamics (radial displacements). (A) Full unsteady dynamics (solid lines) from DNS and theory Eq. 13 and time-averaged dynamics (dashed lines; theory uses Eq. 9 with Eq. 2). The classical MR equation solutions (green) fail to even qualitatively capture the particle attraction to the bubble. (B–E) Steady dynamics from the uniformly valid asymptotic theory agrees with DNS for the entire range of λ values. Dashed lines show the inviscid-limit theory, demonstrating significant quantitative discrepancies, even for the largest λ .

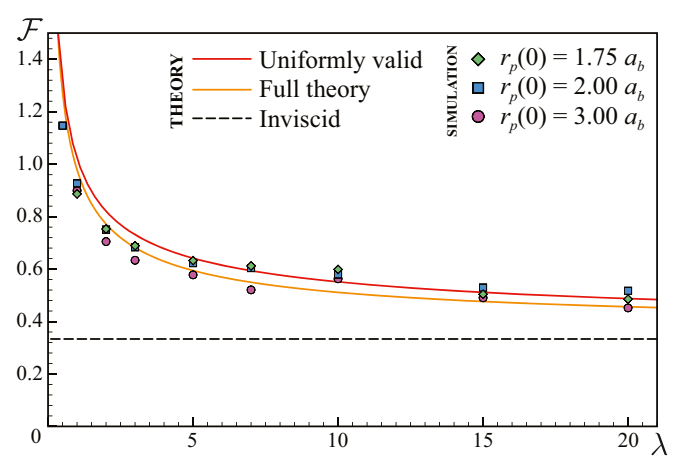


Fig. 4. Comparison of the overall inertial force magnitude \mathcal{F} in theory (lines) and simulation (symbols), for various λ and initial particle positions $r_p(0)$. The uniformly valid expression (red) is extremely close to the full solution (orange) and in excellent agreement with all DNS data, while the inviscid theory (black dashed) severely underestimates the forces.

contributions will not alter or overwhelm the effects described here.

Absence of Outer-Flow Inertia. Often, the evaluation of forces on particles in a flow is complicated by the transition between a viscous-dominated inner flow volume (near the particle) and an inertia-dominated outer volume, necessitating an asymptotic matching of the two limits [such as for the Oseen (2) and Saffman (38) problems]. The present formalism, however, only employs an inner-solution expansion and still obtains accurate predictions (see also ref. 5, where it is shown that such an expansion is successful, even up to $Re_p \sim 10$). This behavior can be rationalized by invoking the analysis of Lovalenti and Brady (2), who showed that an outer region is not present when the characteristic unsteady time scale ω^{-1} is shorter than the convective inertial time scale $\nu/(U^*w^{(0)})^2$, where $w^{(0)}$ is the dimensionless velocity scale of the fluid, as measured in the particle reference frame. For density-matched particles, $w^{(0)} = \mathcal{O}(\alpha)$, so that this criterion reduces to $\epsilon^2 \lambda \ll 1$, requiring the oscillation amplitude of the flow to be smaller than $\delta_S \alpha^{-1}$, which is easily satisfied in most experimental situations. More directly, the Lovalenti-Brady criterion relies on the magnitude of oscillatory inertia in the disturbance flow $\partial w^{(1)}/\partial t$ being much larger than that of the advective term f. DNS verifies that this relation holds for the entire range of λ treated here (Fig. 2 F and H). In flows that do not satisfy this condition, our theory can be applied to both the inner and outer regions, with matching expansions in particle Reynolds number. As a separate effect, outer flow inertia due to the slow (steady) motion of the particle will be present, but only results in $O(\epsilon)$ corrections to the Stokes drag.

Comparison with Other Hydrodynamic Forces. We have investigated the case of radially symmetric flow specifically because it isolates the inertial forces reported here as the only effect, allowing us to assess the accuracy of the theory. In more general flow situations, other forces will compete with $F_{\Gamma\kappa}$, and we estimate their relative magnitude here to show that in many practical scenarios, they will not overwhelm the contributions identified here. If the particle density ρ_p does not match ρ , a density contrast force (19) is induced, generalizing acoustofluidic SRFs. This force is included within our general formalism, but in order for it to exceed $F_{\Gamma\kappa}$, the density contrast needs to fulfill $\rho_p/\rho-1\gtrsim 3(a_p/r_p)^2(1+2/\sqrt{\lambda})$. Appreciable forces only act when $r_p\gtrsim a_b$ and if λ is not very small; thus, $\rho_p/\rho-1\gtrsim 0.3$ for

typical geometries characterized by $\alpha \lesssim 0.2$. In most microfluidic, and certainly in biomedical, applications, the density contrast is far less: Even at 5% density difference (e.g., for polystyrene particles), $F_{\Gamma\kappa}$ is 5 to 30 times stronger than the density contrast force for $0.5 < \lambda < 5$. Other forces result from steady flows: Oscillation of an a_b -sized object will generically induce steadystreaming flow at speed $\sim \epsilon^2 a_b U^*$, and it may have transverse gradients of scale a_b (in addition to radial gradients). This situation induces a Saffman lift force L_S (38) for particles with finite slip velocity V_s , again because of density mismatch (2, 19). Augmenting our theory with an outer-flow inertial region would reproduce this force. † L_S and $F_{\Gamma\kappa}$ are of equal magnitude if $V_s \sim 5\alpha^2 (4.1 + 2\sqrt{\lambda}) U^*$. In realistic settings, V_s would need to exceed U^* , implying that the steady flow would overwhelm the oscillatory motion, defeating the purpose of oscillatory-flow microfluidics. Lastly, flows with finite $\nabla^2 \bar{\mathbf{U}}$ give rise to Faxén terms in added mass and drag. However, the oscillatory flows discussed here are (almost) potential flows, as shown above, so that the leading-order effect of Faxén terms comes from steadyflow curvature and provides only an $\mathcal{O}(\alpha^2)$ correction to the steady-flow Stokes drag.

Conclusions. We thus conclude that the inertial force terms described here are not a small correction, but the dominant effect in many commonplace oscillating microfluidics applications, in particular for nearly density-matched particles, the most relevant case in medicine and health contexts, where biological materials are primary targets. These forces are ubiquitous in viscous flows with finite inertial effects from oscillatory driving; they stem from flow gradients and curvatures; they are attractive toward the oscillating object under mild assumptions; and they are much stronger than inviscid forces. They lead to significant displacements of cell-sized particles $(1-10\mu m)$ over millisecond time scales, making them a promising tool for precision manipulation strategies. Further, our analysis shows that a surprisingly simple expression accurately predicts particle motion, as quantitatively confirmed against first-principle, large-scale DNSs. The theory highlights the immense reduction in computational effort between DNS and an explicit analytical theory and, as a generalization of the Maxey-Riley formalism, is applicable to a wide variety of flow situations.

Materials and Methods

General Solutions and the Reciprocal Theorem. The leading-order oscillatory disturbance flow field $w_0^{(1)}$ is obtained by inserting Eq. 5 into the leading order of Eq. 4 and can be formally expressed as a series solution (41, 42).

$$\boldsymbol{w}_0^{(1)} = \mathcal{M}_D \cdot \boldsymbol{u}_s - \mathcal{M}_Q \cdot (\boldsymbol{r} \cdot \boldsymbol{E}) - \mathcal{M}_Q \cdot (\boldsymbol{rr} \cdot \boldsymbol{G}) + \dots,$$
 [11]

where $u_s = u_{P_0} - \bar{u}|_{r_{P_0}}$ is the slip velocity and $\mathcal{M}_{D,Q,O}(r,\lambda)$ are spatially dependent mobility tensors independent of the particular background flow—*SI Appendix* gives explicit expressions in the case of harmonic oscillatory flows, though the formalism applies for general flows. All information about the specific background flow is contained in the constant quantities u_s , E, and G. The $\mathcal{O}(\text{Re}_p)$ flow field $w_1^{(1)}$ does not need to be computed explicitly; instead, we use a reciprocal theorem. Denoting Laplace-transformed quantities by hats, application of the divergence theorem results in the following symmetry relation:

$$\oint_{S} (\hat{\boldsymbol{w}}_{1}^{(1)} \cdot \hat{\boldsymbol{\sigma}}' - \hat{\boldsymbol{u}}' \cdot \hat{\boldsymbol{\sigma}}_{1}^{(1)}) \cdot \boldsymbol{m} \, dS = \int_{V} \left[\nabla \cdot (\hat{\boldsymbol{w}}_{1}^{(1)} \cdot \hat{\boldsymbol{\sigma}}') - \nabla \cdot (\hat{\boldsymbol{u}}' \cdot \hat{\boldsymbol{\sigma}}_{1}^{(1)}) \right] dV.$$
[12]

As shown in *SI Appendix*, the above expression yields the $\mathcal{O}(\text{Re}_p)$ force on the particle captured by Eq. **6e**. We note that the computation of the volume integral simplifies considerably: The integrand is proportional to f_0 , in which only certain products are nonvanishing when the angular integration around the particle is performed. For

iloaded at UNIV OF CALIFORNIA RIVERSIDE on July 14, 202

[†]We thank H. A. Stone, J. F. Brady, and P. M. Lovalenti for pointing this out.

instance, the first term in f_0 is $(\bar{u} - u_{p_0}) \cdot \nabla w_0^{(1)} = (-u_s + r \cdot E + rr : G) \cdot \nabla (\mathcal{M}_D \cdot u_s - \mathcal{M}_Q \cdot (r \cdot E) - \mathcal{M}_Q \cdot (rr : G)$). Due to the alternating symmetry of terms in the background flow and, consequently, $\boldsymbol{w}_0^{(1)}$, only products of adjacent terms survive integration, while, e.g., a term involving u_s $\nabla \left(\mathcal{M}_{D} \cdot \boldsymbol{u}_{s} \right)$ vanishes after volume integration.

Oscillatory Equation of Motion in Radial Flow. For the special case of the bubble executing pure breathing oscillations with the radial flow field $\bar{u} = \sin t/r^2$, it is straightforward to compute $\mathbf{E} : \mathbf{G} \cdot \mathbf{e}_r = -18 \sin^2 t/r_p^7$, where $r_p(t)$ is the instantaneous particle position.

Using [6], [7], [8], and noting $\alpha \text{Re}_p = 3\epsilon \lambda$, the nondimensional equation of motion for $r_p(t)$ of a neutrally buoyant particle explicitly reads:

$$\begin{split} &\lambda \frac{d^2 r_p}{dt^2} = \epsilon \lambda \left(\frac{\cos t}{r_p^2} - 2\epsilon \frac{\sin^2 t}{r_p^5} \right) - \frac{2\lambda}{3} \epsilon^2 \alpha^2 \frac{18 \sin^2 t}{r_p^7} \mathcal{F}^{(0)} \\ &+ \left[\frac{\sin t}{r_p^2} - \frac{dr_p}{dt} \right] - \left[\frac{2\lambda}{3} \epsilon^2 \alpha^2 \frac{(18 \sin^2 t)}{r_p^7} \mathcal{F}_1^{(1)} \lambda \right], \end{split} \tag{13}$$

where the first line on the right-hand side represents contributions from $F_0^{(0)}$ and $F_1^{(0)}$, while the first and second terms in brackets represent $F_0^{(1)}$ and $F_1^{(1)}$, respectively. Note that, for neutrally buoyant particles, the time-periodic character of the flow precludes memory terms that would otherwise emerge from the inverse Laplace transforms (2, 10, 43).

Time-Scale Separation and Time Averaging. Assuming $\epsilon \ll$ 1, we introduce the slow time $T = \epsilon^2 t$, in addition to the fast time t. Using the following transformations

$$r_p(t)\mapsto r_p(t,T),$$
 [14a]

$$\frac{d}{dt} \mapsto \frac{\partial}{\partial t} + \epsilon^2 \frac{\partial}{\partial T},$$
 [14b]

$$\frac{d}{dt} \mapsto \frac{\partial}{\partial t} + \epsilon^2 \frac{\partial}{\partial T},$$

$$\frac{d^2}{dt^2} \mapsto \frac{\partial^2}{\partial t^2} + 2\epsilon^2 \frac{\partial^2}{\partial t \partial T} + \epsilon^4 \frac{\partial^2}{\partial T^2},$$
[14c]

we seek a perturbation solution in ϵ of the general form $r_p(t, T) = r_p(T) +$ $\epsilon \check{r}_p(t,T) + \epsilon^2 \check{r}_p(t,T) + \dots$ and separate orders in Eq. 13. The procedure is outlined in ref. 19 and results in a leading-order equation for $r_p(T)$ given by Eq. 9, dependent on the slow time scale only (the scale t being averaged

- 1. B. Ho, L. Leal, Inertial migration of rigid spheres in two-dimensional unidirectional flows. J. Fluid Mech. 65, 365-400 (1974).
- 2. P. M. Lovalenti, J. F. Brady, The hydrodynamic force on a rigid particle undergoing arbitrary time-dependent motion at small Reynolds number. J. Fluid Mech. 256, 561-605 (1993).
- J. A. Schonberg, E. Hinch, Inertial migration of a sphere in Poiseuille flow. J. Fluid Mech. 203, 517-524 (1989).
- D. Di Carlo, Inertial microfluidics. Lab Chip 9, 3038-3046 (2009).
- K. Hood, S. Lee, M. Roper, Inertial migration of a rigid sphere in three-dimensional Poiseuille flow. J. Fluid Mech. 765, 452-479 (2015).
- J. Einarsson, F. Candelier, F. Lundell, J. Angilella, B. Mehlig, Effect of weak fluid inertia upon Jeffery orbits. Phys. Rev. 91, 041002 (2015).
- B. R. Lutz, J. Chen, D. T. Schwartz, Hydrodynamic tweezers: 1. Noncontact trapping of single cells using steady streaming microeddies. Anal. Chem. 78, 5429-5435 (2006).
- P. Rogers, A. Neild, Selective particle trapping using an oscillating microbubble. Lab Chip 11, 3710-3715 (2011).
- R. Thameem, B. Rallabandi, S. Hilgenfeldt, Fast inertial particle manipulation in oscillating flows. Phys. Rev. Fluid. 2, 052001 (2017).
- 10. M. R. Maxey, J. J. Riley, Equation of motion for a small rigid sphere in a nonuniform flow. Phys. Fluid. 26, 883-889 (1983).
- E. E. Michaelides, The transient equation of motion for particles, bubbles, and droplets. J. Fluid Eng. 119, 233-247 (1997).
- 12. E. Mograbi, E. Bar-Ziv, On the asymptotic solution of the Maxey-Riley equation. Phys. Fluids 18, 051704 (2006).
- 13. M. Farazmand, G. Haller, The Maxey-Riley equation: Existence, uniqueness and regularity of solutions. Nonlinear Anal. R. World Appl. 22, 98-106 (2015).
- Y. Chen, S. Lee, Manipulation of biological objects using acoustic bubbles: A review. Integr. Comp. Biol. 54, 959-968 (2014).
- S. K. Chung, S. K. Cho, On-chip manipulation of objects using mobile oscillating bubbles. J. Micromech. Microeng. 18, 125024 (2008).
- 16. A. Hashmi, G. Yu, M. Reilly-Collette, G. Heiman, J. Xu, Oscillating bubbles: A versatile tool for lab on a chip applications. Lab Chip 12, 4216-4227 (2012).
- J. H. Shin, J. Seo, J. Hong, S. K. Chung, Hybrid optothermal and acoustic manipulations of microbubbles for precise and on-demand handling of micro-objects. Sensor. Actuator, B Chem. 246, 415-420 (2017).
- Y. Chen et al., Onset of particle trapping and release via acoustic bubbles. Lab Chip 16, 3024-3032 (2016).

out). Higher-order corrections to the irreversible, rectified particle motion only occur at $\mathcal{O}(\epsilon^4)$.

Simulation Method and Numerical Implementation. Here, we briefly describe the governing equations and numerical technique used in our simulations. We consider two spherical bodies (an oscillating microbubble and a neutrally buoyant particle) immersed in an unbounded domain of incompressible viscous fluid. We denote the computational domain as $\Omega = \Omega_f \cup \Omega_B$, where Ω_f is the fluid domain and $\Omega_{\text{B}} = \Omega_{\text{b}} \cup \Omega_{\text{p}}$ is the domain in which the bubble (Ω_b) and particle (Ω_p) reside, and denote the interface between the fluid and the bodies as $\partial\Omega_{\rm B}$. The flow is then described by the incompressible Navier-Stokes equations

$$abla \cdot \boldsymbol{u} = 0, \quad \frac{\partial \boldsymbol{u}}{\partial t} + (\boldsymbol{u} \cdot \boldsymbol{\nabla}) \boldsymbol{u} = -\frac{1}{\rho} \nabla \rho + \nu \boldsymbol{\nabla}^2 \boldsymbol{u} \quad \boldsymbol{x} \in \Omega \setminus \Omega_B,$$
 [15]

where ρ , ${\bf p}$, ${\bf u}$, and ν are the fluid density, pressure, velocity, and kinematic viscosity, respectively. We impose the no-slip boundary condition $u = u_B$ at $\partial\Omega_B$, where u_B is the body velocity, and feedback from the fluid to the body is described by Newton's equation of motion. The system of equations is solved in velocity-vorticity form by using the remeshed vortex method combined with Brinkmann penalization and a projection approach (44). This method has been extensively validated across a range of fluid-structure interaction problems, from flow past bluff bodies to biological swimming (44-48). Recently, the accuracy of this method has been demonstrated in rectified flow contexts as well, capturing steady streaming responses from arbitrary shapes in two dimensions and 3D (39, 40). More details on method implementation and simulation techniques can be found in SI Appendix.

Data Availability. All study data are included in the article and/or SI Appendix.

ACKNOWLEDGMENTS. We thank Kaitlyn Hood, Gabriel Juarez, and Howard A. Stone for fruitful discussions. This work was supported by NSF CAREER Grant CBET-1846752 (to M.G.) and by the Blue Waters project (Grants OCI-0725070 and ACI-1238993), a joint effort of the University of Illinois at Urbana-Champaign and its National Center for Supercomputing Applications. This work also used the Extreme Science and Engineering Discovery Environment Stampede2, supported by NSF Grant ACI-1548562, at the Texas Advanced Computing Center through Allocation TG-MCB190004.

- 19. S. Agarwal, B. Rallabandi, S. Hilgenfeldt, Inertial forces for particle manipulation near oscillating interfaces. Phys. Rev. Fluid. 3, 104201 (2018).
- 20. B. R. Lutz, J. Chen, D. T. Schwartz, Microscopic steady streaming eddies created around short cylinders in a channel: Flow visualization and Stokes layer scaling. Phys. Fluids 17, 023601 (2005).
- 21. C. Wang, S. V. Jalikop, S. Hilgenfeldt, Size-sensitive sorting of microparticles through control of flow geometry. Appl. Phys. Lett. 99,
- 22. L. Schmid, D. A. Weitz, T. Franke, Sorting drops and cells with acoustics: Acoustic microfluidic fluorescence-activated cell sorter. Lab Chip 14, 3710-3718 (2014).
- 23. I. S. Park, J. H. Shin, Y. R. Lee, S. K. Chung, On-chip micromanipulation using a magnetically driven micromanipulator with an acoustically oscillating bubble. Sensor Actuator Phys. 248, 214-222 (2016).
- R. Thameem, B. Rallabandi, S. Hilgenfeldt, Particle migration and sorting in microbubble streaming flows. Biomicrofluidics 10, 014124 (2016).
- A. Volk et al., Size-dependent particle migration and trapping in three-dimensional microbubble streaming flows. Phys. Rev. Fluid. 5, 114201 (2020).
- 26. D. Di Carlo, D. Irimia, R. G. Tompkins, M. Toner, Continuous inertial focusing, ordering, and separation of particles in microchannels. Proc. Natl. Acad. Sci. U.S.A. 104, 18892-18897 (2007)
- 27. M. E. Warkiani et al., Malaria detection using inertial microfluidics. Lab Chip 15, 1101-1109 (2015).
- 28. V. Bjerknes, Fields of Force: Supplementary Lectures, Applications to Meteorology; A Course of Lectures in Mathematical Physics Delivered December 1 to 23, 1905 (Columbia University Press, New York, 1906).
- 29. T. A. Hay, M. F. Hamilton, Y. A. Ilinskii, E. A. Zabolotskaya, Model of coupled pulsation and translation of a gas bubble and rigid particle. J. Acoust. Soc. Am. 125, 1331-1339
- 30. W. T. Coakley, W. Nyborg, "Cavitation; dynamics of gas bubbles; applications" in Ultrasound: Its Applications in Medicine and Biology, F. J. Fry, ed. (Methods and Phenomena: Their Application in Science and Technology, Elsevier, Amsterdam, Netherlands, 1978), vol. 3, pp. 77-159.
- 31. H. Bruus, Acoustofluidics 7: The acoustic radiation force on small particles. Lab Chip 12. 1014-1021 (2012).
- 32. C. Wang, S. V. Jalikop, S. Hilgenfeldt, Efficient manipulation of microparticles in bubble streaming flows. Biomicrofluidics 6, 012801 (2012).

- C. Wang, B. Rallabandi, S. Hilgenfeldt, Frequency dependence and frequency control of microbubble streaming flows. *Phys. Fluids* 25, 022002 (2013).
- 34. M. S. Longuet-Higgins, Viscous streaming from an oscillating spherical bubble. *Proc. R. Soc. Lond. Ser. A: Math. Phys. Eng. Sci.* **454**, 725–742 (1998).
- B. Rallabandi, Inertial forces in the Maxey–Riley equation in nonuniform flows. Phys. Rev. Fluid. 6, L012302 (2021).
- 36. S. Danilov, M. Mironov, Mean force on a small sphere in a sound field in a viscous fluid. *J. Acoust. Soc. Am.* **107**, 143–153 (2000).
- A. Nadim, H. A. Stone, The motion of small particles and droplets in quadratic flows. Stud. Appl. Math. 85, 53–73 (1991).
- 38. P. Saffman, The lift on a small sphere in a slow shear flow. *J. Fluid Mech.* 22, 385–400 (1965).
- T. Parthasarathy, F. K. Chan, M. Gazzola, Streaming-enhanced flow-mediated transport. J. Fluid Mech. 878, 647–662 (2019).
- Y. Bhosale, T. Parthasarathy, M. Gazzola, Shape curvature effects in viscous streaming. J. Fluid Mech. 898, A13 (2020).
- 41. L. D. Landau, E. Lifshitz, *Fluid Mechanies* (Course of Theoretical Physics, Pergamon Press, Oxford, UK, 1959), vol. 6.

- C. Pozrikidis et al., Boundary Integral and Singularity Methods for Linearized Viscous Flow (Cambridge University Press, Cambridge, UK, 1992).
- A. B. Basset, A. Barnard, A Treatise on Hydrodynamics: With Numerous Examples. Vol. 2 (Deighton, Bell and Company, Cambridge, 1888).
- M. Gazzola, P. Chatelain, W. M. Van Rees, P. Koumoutsakos, Simulations of single and multiple swimmers with non-divergence free deforming geometries. *J. Comput. Phys.* 230, 7093–7114 (2011).
- 45. M. Gazzola, C. Mimeau, A. A. Tchieu, P. Koumoutsakos, Flow mediated interactions between two cylinders at finite Re numbers. *Phys. Fluid.* 24, 043103 (2012).
- M. Gazzola, W. M. Van Rees, P. Koumoutsakos, C-start: Optimal start of larval fish. J. Fluid Mech. 698, 5–18 (2012).
- M. Gazzola, B. Hejazialhosseini, P. Koumoutsakos, Reinforcement learning and wavelet adapted vortex methods for simulations of self-propelled swimmers. SIAM J. Sci. Comput. 36, B622–B639 (2014).
- M. Gazzola, A. A. Tchieu, D. Alexeev, A. de Brauer, P. Koumoutsakos, Learning to school in the presence of hydrodynamic interactions. *J. Fluid Mech.* 789, 726–749 (2016).



Supplementary Information for

An unrecognized inertial force induced by flow curvature in microfluidics

Siddhansh Agarwal, Fan Kiat Chan, Bhargav Rallabandi, Mattia Gazzola and Sascha Hilgenfeldt

Corresponding Authors: Sascha Hilgenfeldt, e-mail: sascha@illinois.edu; Mattia Gazzola, e-mail: mgazzola@illinois.edu

This PDF file includes:

Supplementary text Figs. S1 to S4 (not allowed for Brief Reports) SI References

Supporting Information Text

1. Theoretical Formalism

In order to systematically account for the inertial forces on a sphere of radius a_p centered at \mathbf{r}_p moving with with velocity \mathbf{u}_p (neglecting effects of rotation) and exposed to a known (lab-frame) background undisturbed flow $\bar{\mathbf{u}}$, we split the Navier–Stokes equations that govern the flow field into an undisturbed flow $\mathbf{w}^{(0)} = \bar{\mathbf{u}} - \mathbf{u}_p$ and a disturbance flow $\mathbf{w}^{(1)}$ (we adopt the same notation as (1)). Then, in a particle-centered (moving) coordinate system, we have

$$\nabla^2 \boldsymbol{w}^{(0)} - \nabla p^{(0)} = 3\lambda \frac{\partial \boldsymbol{w}^{(0)}}{\partial t} + \operatorname{Re}_p \left(\boldsymbol{w}^{(0)} \cdot \nabla \boldsymbol{w}^{(0)} \right),$$
 [1a]

$$\nabla^{2} \boldsymbol{w}^{(1)} - \nabla p^{(1)} = 3\lambda \frac{\partial \boldsymbol{w}^{(1)}}{\partial t} + \operatorname{Re}_{p} \left[(\bar{\mathbf{u}} - \mathbf{u}_{p}) \cdot \nabla \boldsymbol{w}^{(1)} + \boldsymbol{w}^{(1)} \cdot \nabla \bar{\mathbf{u}} + \boldsymbol{w}^{(1)} \cdot \nabla \boldsymbol{w}^{(1)} \right],$$
 [1b]

$$\nabla \cdot \boldsymbol{w}^{(0)} = 0, \quad \nabla \cdot \boldsymbol{w}^{(1)} = 0,$$
 [1c]

$$\boldsymbol{w}^{(1)} = \mathbf{u}_p - \bar{\mathbf{u}} \quad \text{on } r = 1 \quad \text{and} \quad \boldsymbol{w}^{(1)} = 0 \quad \text{as } r \to \infty,$$
 [1d]

where $\text{Re}_p = U^* a_p / \nu$ is the particle Reynolds number. Quantities in these equations are non-dimensionalized by scaling velocities with U^* , lengths with a_p , pressure with $\mu U^* / a_p$, and time by ω^{-1} .

The force contribution from the undisturbed flow is $\mathbf{F}^{(0)} = (F_S/6\pi) \oint_S \mathbf{n} \cdot \boldsymbol{\sigma}^{(0)} dS$, like in the original Maxey–Riley (MR)

The force contribution from the undisturbed flow is $\mathbf{F}^{(0)} = (F_S/6\pi) \oint_S \mathbf{n} \cdot \boldsymbol{\sigma}^{(0)} dS$, like in the original Maxey–Riley (MR) formalism (1), where $\boldsymbol{\sigma}^{(0)} = -p^{(0)}\mathbf{I} + \nabla \boldsymbol{w}^{(0)} + (\nabla \boldsymbol{w}^{(0)})^T$ is the stress tensor associated with the undisturbed flow field $\boldsymbol{w}^{(0)}$, and $F_S/6\pi = \nu \rho a_p U^*$ is the Stokes drag scale. The force contribution at the disturbance flow order is given by $\mathbf{F}^{(1)} = (F_S/6\pi) \oint_S \mathbf{n} \cdot \boldsymbol{\sigma}^{(1)} dS$, where $\boldsymbol{\sigma}^{(1)} = -p^{(1)}\mathbf{I} + \nabla \boldsymbol{w}^{(1)} + (\nabla \boldsymbol{w}^{(1)})^T$ is the stress tensor associated with the disturbance flow field $\boldsymbol{w}^{(1)}$. The corresponding (dimensional) equation of motion for the particle then reads

$$m_p \frac{d\mathbf{U}_p}{dt} = \mathbf{F}^{(0)} + \mathbf{F}^{(1)}.$$
 [2]

Note that everything up to this point is exact and no assumptions have been made. MR (1) make the unsteady Stokes flow approximation in Eq. (1b) by setting $Re_p = 0$, and compute $\mathbf{F}^{(1)}$ without explicitly evaluating the disturbance flow, using a symmetry relation. While this assumption is plausible in many traditional microfluidic flow situations, fast oscillatory particle motion can give rise to large disturbance flow gradients so that the inertial terms on the RHS of Eq. (1b) are not necessarily negligible compared to the viscous diffusion term (typically $Re_p \sim \mathcal{O}(1)$, as in the experiment described in Fig. 1 of the main text).

A. Small Re_p expansion. In order to make analytical progress, following (2–4), we expand $\mathbf{w}^{(1)}$, $p^{(1)}$, \mathbf{r}_p , \mathbf{u}_p and $\boldsymbol{\sigma}^{(1)}$ (and consequently $\mathbf{F}^{(1)}$) in a regular asymptotic expansion for small Re_p ,

$$\mathbf{w}^{(1)} = \mathbf{w}_0^{(1)} + \operatorname{Re}_p \mathbf{w}_1^{(1)} + \dots,$$
 [3a]

$$p^{(1)} = p_0^{(1)} + \operatorname{Re}_p p_1^{(1)} + \dots,$$
 [3b]

$$\mathbf{r}_p = \mathbf{r}_{p_0} + \operatorname{Re}_p \mathbf{r}_{p_1} + \dots, \tag{3c}$$

$$\mathbf{u}_p = \mathbf{u}_{p_0} + \operatorname{Re}_p \mathbf{u}_{p_1} + \dots, \tag{3d}$$

$$\sigma^{(1)} = \sigma_0^{(1)} + \operatorname{Re}_p \sigma_1^{(1)} + \dots,$$
 [3e]

$$\mathbf{F}^{(1)} = \mathbf{F}_0^{(1)} + \text{Re}_p \, \mathbf{F}_1^{(1)} + \dots$$
 [3f]

The leading-order equations for $(\boldsymbol{w}_0^{(1)}, p_0^{(1)})$ are unsteady Stokes,

$$\nabla^2 \mathbf{w}_0^{(1)} - \nabla p_0^{(1)} = 3\lambda \frac{\partial \mathbf{w}_0^{(1)}}{\partial t},$$
 [4a]

$$\boldsymbol{\nabla} \cdot \boldsymbol{w}_0^{(1)} = 0, \tag{4b}$$

$$\mathbf{w}_0^{(1)} = \mathbf{u}_{p_0} - \bar{\mathbf{u}} \quad \text{on } \mathbf{r} = 1,$$
 [4c]

$$\mathbf{w}_0^{(1)} = 0 \quad \text{as } \mathbf{r} \to \infty.$$
 [4d]

We note that in the original derivation of MR (1), a symmetry relation was used at this order to compute $\mathbf{F}_0^{(1)}$ without explicitly solving for $\boldsymbol{w}_0^{(1)}$. However, since we are interested in computing the force contribution at $\mathcal{O}(\text{Re}_p)$, we need an explicit solution for the leading-order disturbance flow $\boldsymbol{w}_0^{(1)}$. To obtain explicit results, as stated in the main text, we expand the background flow field $\bar{\mathbf{u}}$ around the leading-order particle position \mathbf{r}_{p_0} into spatial moments of alternating symmetry,

$$\bar{\mathbf{u}} = \bar{\mathbf{u}}|_{\mathbf{r}_{p_0}} + \mathbf{r} \cdot \mathbf{E} + \mathbf{r}\mathbf{r} : \mathbf{G} + \dots, \tag{5}$$

where $\mathbf{E} = (a_p/L_\Gamma)\nabla \bar{\mathbf{u}}|_{\mathbf{r}_{p_0}}$ and $\mathbf{G} = \frac{1}{2}(a_p^2/L_\kappa^2)\nabla\nabla \bar{\mathbf{u}}|_{\mathbf{r}_{p_0}}$ with gradient L_Γ and curvature L_κ length scales. As a consequence of Eq. (5), the boundary condition Eq. (4c) is also expanded around \mathbf{r}_{p_0} , so that in the particle fixed coordinate system

$$\mathbf{w}_0^{(1)} = \mathbf{u}_{p_0} - \bar{\mathbf{u}} = \mathbf{u}_{p_0} - \bar{\mathbf{u}}|_{\mathbf{r}_{p_0}} - \mathbf{r} \cdot \mathbf{E} - \mathbf{r}\mathbf{r} : \mathbf{G} + \dots \quad \text{on} \quad \mathbf{r} = 1,$$
 [6]

where we have retained the first three terms in the background flow velocity expansion. Owing to the linearity of the leading order unsteady Stokes equation, the solution can generally be expressed as (5,6)

$$\boldsymbol{w}_0^{(1)} = \boldsymbol{\mathcal{M}}_D \cdot \mathbf{u}_s - \boldsymbol{\mathcal{M}}_Q \cdot (\mathbf{r} \cdot \mathbf{E}) - \boldsymbol{\mathcal{M}}_Q \cdot (\mathbf{rr} : \mathbf{G}) + \dots,$$
 [7]

where $\mathcal{M}_{D,Q,O}(r,\lambda)$ are spatially dependent mobility tensors. For oscillatory flows, they depend on the Stokes number λ . More explicit forms of these tensors will be given below.

With the leading-order disturbance flow field known, the equations at $\mathcal{O}(\text{Re}_p)$ are as follows,

$$\nabla^2 \mathbf{w}_1^{(1)} - \nabla p_1^{(1)} = \nabla \cdot \mathbf{\sigma}_1^{(1)} = 3\lambda \frac{\partial \mathbf{w}_1^{(1)}}{\partial t} + \mathbf{f}_0,$$
 [8a]

$$\nabla \cdot \boldsymbol{w}_{1}^{(1)} = 0, \tag{8b}$$

$$\mathbf{w}_1^{(1)} = \mathbf{u}_{p_1} \quad \text{on } \mathbf{r} = 1,$$
 [8c]

$$\mathbf{w}_{1}^{(1)} = 0 \quad \text{as } \mathbf{r} \to \infty,$$
 [8d]

where $\mathbf{f}_0 = \boldsymbol{w}^{(0)} \cdot \nabla \boldsymbol{w}_0^{(1)} + \boldsymbol{w}_0^{(1)} \cdot \nabla \boldsymbol{w}^{(0)} + \boldsymbol{w}_0^{(1)} \cdot \nabla \boldsymbol{w}_0^{(1)}$ is the (explicitly known) leading-order nonlinear forcing of the disturbance flow. In order to compute the force at this order, we employ a reciprocal relation in the Laplace domain since the problem is time-dependent and, for oscillatory flows, the Laplace transform is explicitly obtained.

B. Reciprocal theorem and test flow. A known test flow (denoted by primed quantities such as \mathbf{u}') is chosen around an oscillating sphere such that it satisfies the following unsteady Stokes equation:

$$\nabla^2 \mathbf{u}' - \nabla p' = \nabla \cdot \boldsymbol{\sigma}' = 3\lambda \frac{\partial \mathbf{u}'}{\partial t},$$
 [9a]

$$\nabla \cdot \mathbf{u}' = 0, ag{9b}$$

$$\mathbf{u}' = u'(t)\,\mathbf{e} \quad \text{on } \mathbf{r} = 1,$$
 [9c]

$$\mathbf{u}' = 0 \quad \text{as } \mathbf{r} \to \infty,$$
 [9d]

where the unit vector **e** is chosen to coincide with the direction in which the force on the particle is desired. The solution to this problem is of the same form as Eq. (7), but with only the first term, i.e.,

$$\mathbf{u}' = u'(t)\mathcal{M}_D \cdot \mathbf{e} \,. \tag{10}$$

Denoting Laplace transformed quantities by hats (e.g., $\hat{\mathbf{u}}$), one can write down the following symmetry relation using the divergence theorem (cf. (1, 4, 7)):

$$\oint_{S} (\hat{\boldsymbol{w}}_{1}^{(1)} \cdot \hat{\boldsymbol{\sigma}}' - \hat{\mathbf{u}}' \cdot \hat{\boldsymbol{\sigma}}_{1}^{(1)}) \cdot \mathbf{m} \, dS = \int_{V} \left[\nabla \cdot (\hat{\boldsymbol{w}}_{1}^{(1)} \cdot \hat{\boldsymbol{\sigma}}') - \nabla \cdot (\hat{\mathbf{u}}' \cdot \hat{\boldsymbol{\sigma}}_{1}^{(1)}) \right] dV, \tag{11}$$

where **m** is the outward unit normal vector to the surface (pointing inward over the sphere surface), and $\hat{\boldsymbol{\sigma}} = \nabla \hat{\mathbf{u}} + (\nabla \hat{\mathbf{u}})^T - \hat{p}\mathbf{I}$. Substituting boundary conditions from Eq. (8) and Eq. (9), and setting the volume equal to the fluid-filled domain, we obtain

$$\hat{\mathbf{u}}_{p_{1}}^{(1)} \cdot \int_{S_{p}} (\hat{\boldsymbol{\sigma}}' \cdot \mathbf{m}) dS - \hat{u}' \mathbf{e} \cdot \int_{S_{p}} (\hat{\boldsymbol{\sigma}}_{1}^{(1)} \cdot \mathbf{m}) dS + \int_{S_{\infty}} (\hat{\boldsymbol{w}}_{1}^{(1)} \cdot \hat{\boldsymbol{\sigma}}') \cdot \mathbf{m} dS - \int_{S_{\infty}} (\hat{\mathbf{u}}' \cdot \hat{\boldsymbol{\sigma}}_{1}^{(1)}) \cdot \mathbf{m} dS
= \int_{V} \left[\hat{\boldsymbol{w}}_{1}^{(1)} \cdot (\nabla \cdot \hat{\boldsymbol{\sigma}}') - \hat{\mathbf{u}}' \cdot (\nabla \cdot \hat{\boldsymbol{\sigma}}_{1}^{(1)}) + \nabla \hat{\boldsymbol{w}}_{1}^{(1)} : \hat{\boldsymbol{\sigma}}' - \nabla \hat{\mathbf{u}}' : \hat{\boldsymbol{\sigma}}_{1}^{(1)} \right] dV.$$
[12]

The third term on the LHS is 0 since the viscous test flow stress tensor decays to zero at infinity. Similarly, the integral in the fourth term vanishes in the far field if viscous stresses dominate inertial terms, and also in the case of inviscid irrotational flows (see (7, 8)). The third and fourth terms on the RHS also go to zero, owing to incompressibilty and symmetry of the stress tensor:

$$\nabla \hat{\boldsymbol{w}}_{1}^{(1)} : \hat{\boldsymbol{\sigma}}' - \nabla \hat{\mathbf{u}}' : \hat{\boldsymbol{\sigma}}_{1}^{(1)}$$

$$= \nabla \hat{\boldsymbol{w}}_{1}^{(1)} : (\nabla \hat{\mathbf{u}}' + (\nabla \hat{\mathbf{u}}')^{T}) - \hat{p}' \nabla \cdot \hat{\boldsymbol{w}}_{1}^{(1)} - \nabla \hat{\mathbf{u}}' : (\nabla \hat{\boldsymbol{w}}_{1}^{(1)} + (\nabla \hat{\boldsymbol{w}}_{1}^{(1)})^{T}) - \hat{p}^{(1)} \nabla \cdot \hat{\mathbf{u}}' = 0.$$
[13]

The divergence of the hatted stress tensors in the remaining two terms of the RHS can be obtained by taking the Laplace transforms of Eq. (8) and Eq. (9) and using the property $\widehat{f'(t)} = \widehat{sf(t)} - f(0)$, so that

$$\nabla \cdot \hat{\boldsymbol{\sigma}}' = \bar{\lambda} s \hat{\mathbf{u}}' - \mathbf{u}'(0), \tag{14a}$$

$$\nabla \cdot \hat{\boldsymbol{\sigma}}_{1}^{(1)} = \bar{\lambda} s \hat{\boldsymbol{w}}_{1}^{(1)} - \boldsymbol{w}_{1}^{(1)}(0) + \hat{\mathbf{f}}_{0}.$$
 [14b]

Now, the force on the sphere at this order is given by $\mathbf{F}_1^{(1)} = \int_{S_p} (\boldsymbol{\sigma}_1^{(1)} \cdot \mathbf{n}) dS = -\int_{S_p} (\boldsymbol{\sigma}_1^{(1)} \cdot \mathbf{m}) dS$, since **m** points inwards while **n** points outwards on the surface of the sphere. Assuming both flows start from rest, we have (cf. (7))

$$\hat{u}'\mathbf{e} \cdot \frac{\hat{\mathbf{F}}_{1}^{(1)}}{F_{S}/(6\pi)} = \hat{\mathbf{u}}_{p_{1}} \cdot \int_{S_{p}} (\hat{\boldsymbol{\sigma}}' \cdot \mathbf{n}) dS - \int_{V} \hat{\mathbf{u}}' \cdot \hat{\mathbf{f}}_{0} dV + \mathcal{O}(\operatorname{Re}_{p}^{2}).$$
 [15]

Adding the force contribution from the previous order, the net force on the particle due to its disturbance flow reads

$$\hat{u}' \mathbf{e} \cdot \frac{\hat{\mathbf{F}}^{(1)}}{F_S/(6\pi)} = \hat{u}' \mathbf{e} \cdot \left(\hat{\mathbf{F}}_0^{(1)} + \operatorname{Re}_p \hat{\mathbf{F}}_1^{(1)}\right) + \mathcal{O}(\operatorname{Re}_p^2)$$

$$= \int_{S_p} \left(\hat{\mathbf{u}}_{p_0} - \hat{\mathbf{u}} + \operatorname{Re}_p \hat{\mathbf{u}}_{p_1}\right) \cdot (\hat{\boldsymbol{\sigma}}' \cdot \mathbf{n}) dS - \operatorname{Re}_p \int_V \hat{\mathbf{u}}' \cdot \hat{\mathbf{f}}_0 dV + \mathcal{O}(\operatorname{Re}_p^2)$$
[16a]

$$\implies \mathbf{e} \cdot \mathbf{F}^{(1)} = \frac{F_S}{6\pi} \mathcal{L}^{-1} \left\{ \int_{S_p} \frac{\left(\hat{\mathbf{u}}_p - \hat{\bar{\mathbf{u}}}\right)}{\hat{u}'} \cdot (\hat{\boldsymbol{\sigma}}' \cdot \mathbf{n}) dS - \frac{1}{\hat{u}'} \operatorname{Re}_p \int_V \hat{\mathbf{u}}' \cdot \hat{\mathbf{f}}_0 dV \right\} + \mathcal{O}(\operatorname{Re}_p^2), \tag{16b}$$

where we have used $\mathbf{u}_p = \mathbf{u}_{p_0} + \operatorname{Re}_p \mathbf{u}_{p_1} + \mathcal{O}(\operatorname{Re}_p^2)$, and \mathcal{L}^{-1} denotes the inverse Laplace transform. The first term on the RHS of Eq. (16b) is denoted as $F_0^{(1)}$ in the main text (and is the same as that obtained by MR), while the second term represents the $\mathcal{O}(\operatorname{Re}_p)$ inertial force and is denoted as $F_1^{(1)}$ in the main text.

2. Evaluation of the $\mathcal{O}(\mathrm{Re}_p)$ inertial force

In this section, we will explicitly evaluate the volume integral in Eq. (16b) representing the $\mathcal{O}(\text{Re}_p)$ inertial force. This requires obtaining \mathbf{f}_0 from the leading-order oscillatory disturbance flow field $\boldsymbol{w}_0^{(1)}$.

A. General solution to equation Eq. (4). We already remarked that, given the background flow field expansion in uniform, linear, and quadratic parts around the particle, $\boldsymbol{w}_0^{(1)}$ is formally obtained as the linear combination Eq. (7). For harmonically oscillating, axisymmetric background flows (i.e., $\bar{\mathbf{u}}(\mathbf{r}) = \{\bar{u}_r, \bar{u}_\theta, 0\}$ in the spherical particle coordinate system, with all components $\propto e^{it}$), general explicit expressions can be derived for the mobility tensors $\mathcal{M}_{D,Q,O}$, ensuring no-slip boundary conditions on the sphere order-by-order. A procedure obtaining \mathcal{M}_D is described in Landau–Lifshitz (5); the other tensors are determined analogously. Using components in spherical coordinates, they read

$$\mathcal{M}_{D} = \begin{bmatrix} \frac{2a(r)}{r^{2}} & 0 & 0\\ 0 & \frac{a'(r)}{r} & 0\\ 0 & 0 & 0 \end{bmatrix}, \quad \mathcal{M}_{Q} = \begin{bmatrix} \frac{b(r)}{r^{3}} & 0 & 0\\ 0 & \frac{b'(r)}{3r^{2}} & 0\\ 0 & 0 & 0 \end{bmatrix}, \quad \mathcal{M}_{O} = \begin{bmatrix} \frac{-32c(r)}{3r^{4}} & 0 & 0\\ 0 & \frac{8c'(r)}{3r^{3}} & 0\\ 0 & 0 & 0 \end{bmatrix},$$
[17]

where

$$a(r) = \frac{1}{2\beta^2 r} \left[\beta^2 - 3i\beta + 3 - 3e^{-i\beta(r-1)} (1 + i\beta r) \right],$$
 [18a]

$$b(r) = \frac{1}{\beta^2(\beta - i)r^2} \left[\beta(-15 + \beta(\beta - 6i)) + 15i + 5e^{-i\beta(r-1)} (\beta r(3 + i\beta r) - 3i) \right],$$
 [18b]

$$c(r) = \frac{-3(105 + \beta(\beta(-45 + \beta(\beta - 10i)) + 105i)) + 21e^{-i\beta(r-1)}(15 + \beta r(-\beta r(6 + i\beta r) + 15i))}{32\beta^2(-3 + \beta(\beta - 3i))r^3},$$
 [18c]

and $\beta = \sqrt{-ia_p^2/(\nu/\omega)} = \sqrt{-3i\lambda}$ is the complex oscillatory boundary layer thickness. We emphasize that these expressions are the same for arbitrary axisymmetric oscillatory $\bar{\bf u}$. Accordingly, only the expansion coefficients ${\bf u}_s$, ${\bf E}$, and ${\bf G}$ contain information about the particular flow.

Similarly, the solution to the unsteady test flow is obtained directly as

$$\mathbf{u}' = \mathcal{M}_D \cdot \begin{bmatrix} \cos \theta \\ -\sin \theta \\ 0 \end{bmatrix} e^{it} \,. \tag{19}$$

It is understood everywhere that physical quantities are obtained by taking real parts of these complex functions.

B. Evaluation of $F_1^{(1)}$. In order to compute the volume integral in Eq. (16b), we first note that only certain products in \mathbf{f}_0 are non-vanishing when the angular integration over θ is performed. In particular, due to alternating symmetry of terms in the background flow field expansion Eq. (5), and consequently in the leading order disturbance flow Eq. (7), only products of adjacent terms survive. This is because, in the Taylor expansion of the background flow field, the first and third terms are symmetric $(\mathbf{u}(-\mathbf{r}) = \mathbf{u}(\mathbf{r}))$ while the second one is anti-symmetric $(\mathbf{u}(-\mathbf{r}) = -\mathbf{u}(\mathbf{r}))$. For example, the first term in \mathbf{f}_0 reads

$$\boldsymbol{w}^{(0)} \cdot \nabla \boldsymbol{w}_0^{(1)} = (-\mathbf{u}_s + \mathbf{r} \cdot \mathbf{E} + \mathbf{rr} : \mathbf{G}) \cdot \nabla \left(\mathcal{M}_D \cdot \mathbf{u}_s - \mathcal{M}_Q \cdot (\mathbf{r} \cdot \mathbf{E}) - \mathcal{M}_O \cdot (\mathbf{rr} : \mathbf{G}) \right),$$
[20]

and the only terms that survive the angular integration are the symmetric ones (after a contraction with the symmetric test flow \mathbf{u}'), i.e.,

$$(-\mathbf{u}_s + \mathbf{rr} : \mathbf{G}) \cdot \nabla (-\mathcal{M}_Q \cdot (\mathbf{r} \cdot \mathbf{E})) + (\mathbf{r} \cdot \mathbf{E}) \cdot \nabla (\mathcal{M}_D \cdot \mathbf{u}_s - \mathcal{M}_O \cdot (\mathbf{rr} : \mathbf{G})) .$$
 [21]

Furthermore, in this paper we restrict ourselves to the case of neutrally buoyant particles and consequently the slip velocity is $\mathbf{u}_s = 0$. In summary, only the following terms in \mathbf{f}_0 have non-trivial contributions to the volume integral:

$$\mathbf{f}_{0} = -\left(\mathbf{r}\mathbf{r}:\mathbf{G}\right) \cdot \nabla\left(\mathcal{M}_{Q} \cdot \left(\mathbf{r} \cdot \mathbf{E}\right)\right) - \left(\mathbf{r} \cdot \mathbf{E}\right) \cdot \nabla\left(\mathcal{M}_{Q} \cdot \left(\mathbf{r}\mathbf{r}:\mathbf{G}\right)\right) \\
- \left(\mathcal{M}_{Q} \cdot \left(\mathbf{r} \cdot \mathbf{E}\right)\right) \cdot \nabla\left(\mathbf{r}\mathbf{r}:\mathbf{G}\right) - \left(\mathcal{M}_{Q} \cdot \left(\mathbf{r}\mathbf{r}:\mathbf{G}\right)\right) \cdot \nabla\left(\mathbf{r} \cdot \mathbf{E}\right) \\
+ \left(\mathcal{M}_{Q} \cdot \left(\mathbf{r} \cdot \mathbf{E}\right)\right) \cdot \nabla\left(\mathcal{M}_{Q} \cdot \left(\mathbf{r}\mathbf{r}:\mathbf{G}\right)\right) + \left(\mathcal{M}_{Q} \cdot \left(\mathbf{r}\mathbf{r}:\mathbf{G}\right)\right) \cdot \nabla\left(\mathcal{M}_{Q} \cdot \left(\mathbf{r} \cdot \mathbf{E}\right)\right).$$
[22]

All information about the background flow field is contained in the constant tensors \mathbf{E} and \mathbf{G} , which are evaluated at the particle position. If the particle is farther away from the surface of the oscillating object exciting the flow than the Stokes layer thickness δ_S , it is exposed to a pure potential flow; this will be the case in the overwhelming majority of realistic scenarios. For potential flows it can be shown that all non-zero terms of Eq. (22) are proportional to $\mathbf{E} : \mathbf{G}$. Choosing a test flow in direction \mathbf{e} , one obtains a surprisingly compact result for the \mathbf{e} -component of the $\mathcal{O}(\mathrm{Re}_p)$ inertial force:

$$\left\langle \frac{F_1^{(1)}}{F_S} \right\rangle = -\frac{1}{6\pi} \left\langle \mathcal{L}^{-1} \left\{ \frac{1}{\hat{u}'} \int_V \hat{\mathbf{u}}' \cdot \hat{\mathbf{f}}_0 dV \right\} \right\rangle = \frac{4}{9} \langle \mathbf{E} : \mathbf{G} \rangle \cdot \mathbf{e} \, \mathcal{F}_1^{(1)}(\lambda) \,. \tag{23}$$

We have here applied the required Laplace transforms as well as a time average to extract the steady part of the force. Performing the volume integral leaves a universal dimensionless function $\mathcal{F}(\lambda)$, whose contributions stem from $\mathcal{M}_{D,Q,O}$. Explicitly, this function reads

$$\begin{split} \mathcal{F}_{1}^{(1)}(\lambda) &= \left[2\pi \bigg(-796500\bar{\lambda}^{3/2} - 336636\bar{\lambda}^{5/2} + 34005\bar{\lambda}^{7/2} + 59790\bar{\lambda}^{9/2} + 3312\bar{\lambda}^{11/2} + 568\bar{\lambda}^{6} \right. \\ &+ 14078\bar{\lambda}^{5} + 97470\bar{\lambda}^{4} - 109920\bar{\lambda}^{3} - 646137\bar{\lambda}^{2} - 648594\bar{\lambda} - 322056\sqrt{\bar{\lambda}} - 76545 \bigg) \\ &+ e^{(1-i)\sqrt{\bar{\lambda}}}\pi\bar{\lambda}^{5/2} \bigg(9 \bigg(\pi(4410 + 2033i) - 28176e^{(1+i)\sqrt{\bar{\lambda}}} \mathrm{Ei} \left(-2\sqrt{\bar{\lambda}} \right) + e^{(2+2i)\sqrt{\bar{\lambda}}} (5600 - 12600i) \mathrm{Ei} \left((-3-i)\sqrt{\bar{\lambda}} \right) \\ &- (2033 + 4410i)e^{2i\sqrt{\bar{\lambda}}} \mathrm{Ei} \left((-1-i)\sqrt{\bar{\lambda}} \right) + e^{2\sqrt{\bar{\lambda}}} (5600 + 12600i) \mathrm{Ei} \left((-3+i)\sqrt{\bar{\lambda}} \right) - (2033 - 4410i) \mathrm{Ei} \left((-1+i)\sqrt{\bar{\lambda}} \right) \\ &+ e^{(2+2i)\sqrt{\bar{\lambda}}} (12600 + 5600i)\pi + e^{2i\sqrt{\bar{\lambda}}} (4410 - 2033i)\pi + e^{2\sqrt{\bar{\lambda}}} (12600 - 5600i)\pi \bigg) \bar{\lambda}^{3/2} + 6 \bigg(\pi(4195 + 3982i) \\ &- 28080e^{(1+i)\sqrt{\bar{\lambda}}} \mathrm{Ei} \left(-2\sqrt{\bar{\lambda}} \right) - (3982 + 4195i)e^{2i\sqrt{\bar{\lambda}}} \mathrm{Ei} \left((-1-i)\sqrt{\bar{\lambda}} \right) - (3982 - 4195i) \mathrm{Ei} \left((-1+i)\sqrt{\bar{\lambda}} \right) \\ &+ e^{2i\sqrt{\bar{\lambda}}} (4195 - 3982i)\pi \bigg) \bar{\lambda}^{5/2} + 4 \bigg(\pi(241 + 1714i) + 720e^{(1+i)\sqrt{\bar{\lambda}}} \mathrm{Ei} \left(-2\sqrt{\bar{\lambda}} \right) - (1714 + 241i)e^{2i\sqrt{\bar{\lambda}}} \mathrm{Ei} \left((-1+i)\sqrt{\bar{\lambda}} \right) + e^{2i\sqrt{\bar{\lambda}}} (241 - 1714i)\pi \bigg) \bar{\lambda}^{7/2} - (120 + 120i) \bigg(\pi \left(-i + e^{2i\sqrt{\bar{\lambda}}} \right) - ie^{2i\sqrt{\bar{\lambda}}} \mathrm{Ei} \left((-1-i)\sqrt{\bar{\lambda}} \right) \\ &+ \mathrm{Ei} \left((-1+i)\sqrt{\bar{\lambda}} \right) \bar{\lambda}^{9/2} - (4+4i) \bigg(\pi \left(e^{2i\sqrt{\bar{\lambda}}} (248 + 127i) + (-127 - 248i) \right) + e^{2i\sqrt{\bar{\lambda}}} (127 - 248i) \mathrm{Ei} \left((-1-i)\sqrt{\bar{\lambda}} \right) \\ &+ (248 - 127i) \mathrm{Ei} \left((-1+i)\sqrt{\bar{\lambda}} \right) \bar{\lambda}^{4} - (6+6i) \bigg(e^{2i\sqrt{\bar{\lambda}}} \pi(567 + 2134i) + e^{(1+i)\sqrt{\bar{\lambda}}} (736 - 736i) \mathrm{Ei} \left(-2\sqrt{\bar{\lambda}} \right) \\ &+ e^{2i\sqrt{\bar{\lambda}}} (2134 - 567i) \mathrm{Ei} \left((-1-i)\sqrt{\bar{\lambda}} \right) + (567 - 2134i) \mathrm{Ei} \left((-1+i)\sqrt{\bar{\lambda}} \right) + (-2134 - 567i)\pi \bigg) \bar{\lambda}^{3} \\ &+ \bigg(\pi(39033 + 25089i) - 381504e^{(1+i)\sqrt{\bar{\lambda}}} \mathrm{Ei} \left(-2\sqrt{\bar{\lambda}} \right) - (25089 + 39033i) e^{2i\sqrt{\bar{\lambda}}} \mathrm{Ei} \left((-1-i)\sqrt{\bar{\lambda}} \right) \bigg) \bigg)$$

$$-(25089 - 39033i) \text{Ei} \left((-1+i)\sqrt{\bar{\lambda}} \right) + e^{2i\sqrt{\bar{\lambda}}} (39033 - 25089i)\pi \right) \bar{\lambda}^{2} + (315 + 315i) \left(e^{(2+2i)\sqrt{\bar{\lambda}}} \pi (420 + 60i) - (96 - 96i)e^{(1+i)\sqrt{\bar{\lambda}}} \text{Ei} \left(-2\sqrt{\bar{\lambda}} \right) + e^{(2+2i)\sqrt{\bar{\lambda}}} (60 - 420i) \text{Ei} \left((-3-i)\sqrt{\bar{\lambda}} \right) - (49 + 28i)e^{2i\sqrt{\bar{\lambda}}} \text{Ei} \left((-1-i)\sqrt{\bar{\lambda}} \right) + e^{2\sqrt{\bar{\lambda}}} (420 - 60i) \text{Ei} \left((-3+i)\sqrt{\bar{\lambda}} \right) + (28 + 49i) \text{Ei} \left((-1+i)\sqrt{\bar{\lambda}} \right) - (60 + 420i)e^{2\sqrt{\bar{\lambda}}} \pi + (49 - 28i)\pi + e^{2i\sqrt{\bar{\lambda}}} (28 - 49i)\pi \right) \bar{\lambda} + 15120e^{\sqrt{\bar{\lambda}}} \left(-5ie^{\sqrt{\bar{\lambda}}} \pi + 5ie^{(1+2i)\sqrt{\bar{\lambda}}} \pi + 5e^{(1+2i)\sqrt{\bar{\lambda}}} \text{Ei} \left((-3-i)\sqrt{\bar{\lambda}} \right) + 5e^{\sqrt{\bar{\lambda}}} \text{Ei} \left((-3+i)\sqrt{\bar{\lambda}} \right) - e^{i\sqrt{\bar{\lambda}}} \text{Ei} \left((-3+i)\sqrt{\bar{\lambda}} \right) + 945 \left(7\pi + 7e^{2i\sqrt{\bar{\lambda}}} \pi - 160ie^{2\sqrt{\bar{\lambda}}} \pi + 160ie^{(2+2i)\sqrt{\bar{\lambda}}} \pi + 160e^{(2+2i)\sqrt{\bar{\lambda}}} \text{Ei} \left((-3-i)\sqrt{\bar{\lambda}} \right) + 160e^{2\sqrt{\bar{\lambda}}} \text{Ei} \left((-3+i)\sqrt{\bar{\lambda}} \right) - 48e^{(1+i)\sqrt{\bar{\lambda}}} \text{Ei} \left((-2\sqrt{\bar{\lambda}}) - 7ie^{2i\sqrt{\bar{\lambda}}} \text{Ei} \left((-1-i)\sqrt{\bar{\lambda}} \right) + 7i \text{Ei} \left((-1+i)\sqrt{\bar{\lambda}} \right) \right) \sqrt{\bar{\lambda}} \right) \right] \right/ \left[15120\sqrt{\bar{\lambda}} \left(84\bar{\lambda}^{3/2} + 32\bar{\lambda}^{5/2} + 8\bar{\lambda}^{3} + 64\bar{\lambda}^{2} + 72\bar{\lambda} + 36\sqrt{\bar{\lambda}} + 9 \right) \right].$$

Here $\bar{\lambda} = (3/2)\lambda$ and Ei is the exponential integral function. We show below that this lengthy expression is approximated to great accuracy by two simple terms.

We stress again here that the result is universal for any oscillatory potential flow; for the prototypical case of the volumetrically oscillating bubble, $\langle \mathbf{E} : \mathbf{G} \rangle \cdot \mathbf{e}_r = -9/r_p^7$, as noted in the Methods section.

C. Net inertial force. The time-averaged force contribution from the background flow at $\mathcal{O}(\text{Re}_p)$ is of the same form as Eq. (23), except that $\mathcal{F}(\lambda)$ is replaced by the simple constant $\mathcal{F}_1^{(0)} = \frac{1}{5}$ (9). The two contributions $F_1^{(1)}$ and $F_1^{(0)}$ can thus be simply added. Transforming back to dimensional variables, we obtain the net time-averaged force on the particle as

$$\mathbf{F}_{\Gamma\kappa} = m_f a_p^2 \left\langle \nabla \bar{\mathbf{U}} : \nabla \nabla \bar{\mathbf{U}} \right\rangle \mathcal{F}(\lambda), \tag{25}$$

where $\mathcal{F} = \mathcal{F}_1^{(1)} + \mathcal{F}_1^{(0)}$ and $m_f = 4\pi \rho a_p^3/3$, as noted in the main text. This time-averaged inertial force on the particle is derived for a background flow that is symmetric about an axis **e** passing through the center of the particle.

It was remarked above that the simple form of Eq. (25) is a consequence of the background flow being potential. This can be backed up by symmetry arguments and dimensional analysis for an arbitrary oscillatory background flow that has a harmonic scalar potential, $\bar{\mathbf{U}} = \nabla \bar{\varphi}$ with $\nabla^2 \bar{\varphi} = 0$. Such a flow is in fact generic since the background flow vorticity decays exponentially outside the Stokes boundary layer of the compact object driving the background flow. We are interested in a time-averaged force on the particle that is (i) quadratic in the oscillation amplitude and (ii) involves contractions of the flow gradient $\nabla \bar{\mathbf{U}} = \nabla \nabla \bar{\varphi}$ and the flow curvature tensor $\nabla \nabla \bar{\mathbf{U}} = \nabla \nabla \nabla \bar{\varphi}$. The only dimensionless parameter in the problem not already specified by $\bar{\mathbf{U}}$ is the Stokes number λ . Collecting the above statements, the only way to construct the time-averaged force (a vector) from the higher rank tensors $\nabla \nabla \bar{\varphi}$ and $\nabla \nabla \nabla \bar{\varphi}$ is by their contraction $\nabla \nabla \bar{\varphi} : \nabla \nabla \nabla \bar{\varphi}$. All other combinations are either of insufficient tensor rank or are identically zero (since $\nabla^2 \bar{\varphi} = 0$). See (10) for similar arguments for flows without curvature. Including the correct dimensions, the time averaged force for any oscillatory potential background flow thus has the form

$$\mathbf{F}_{\Gamma\kappa} = m_f a_p^2 \left\langle \nabla \nabla \bar{\varphi} : \nabla \nabla \nabla \bar{\varphi} \right\rangle \mathcal{F}(\lambda) \,. \tag{26}$$

Note that although the background flow is irrotational, the disturbance flow has a finite vorticity within the Stokes layer around the particle. Under this general setting there is no requirement of axisymmetry of the background flow, so Eq. (25) as well as (1) in the main text apply to the generic case of an oscillatory potential flow background, and with the same universal function $\mathcal{F}(\lambda)$.

3. Accuracy of the uniformly valid expression for $\ensuremath{\mathcal{F}}$

As stated in the main text, while the explicit functional form Eq. (24) of $\mathcal{F}_1^{(1)}(\lambda)$ is rather lengthy, we Taylor expand in both the viscously dominated limit $(\lambda \to 0)$ and the inviscid limit $(\lambda \to \infty)$ to obtain

$$\mathcal{F}^{v} = \frac{9}{16} \sqrt{\frac{3}{2\lambda}} + \mathcal{O}(1), \quad \mathcal{F}^{i} = \frac{1}{3} + \mathcal{O}(1/\sqrt{\lambda}). \tag{27}$$

We construct a uniformly valid solution by simply adding the two leading order results, yielding $\mathcal{F}(\lambda) = \frac{1}{3} + \frac{9}{16}\sqrt{\frac{3}{2\lambda}}$. In Fig. S1(a), we plot the uniformly valid \mathcal{F} (red curve) and the full theory represented by Eq. Eq. (24) (orange), along with the viscous and inviscid limits denoted by dashed lines. Figure S1(b) shows that the relative error between the red and orange curves is small ($\lesssim 8\%$) for all λ , even those far smaller or larger than practically relevant values.

4. Fitting procedure to obtain \mathcal{F} from DNS

The DNS outputs (unsteady) particle trajectories as a function of time, with an initial transient period when the particle starts from rest before periodic motion is fully established. As shown in Fig. 3(a) of the main text, these oscillatory trajectories were time-averaged to obtain the steady particle dynamics $r_p(T)$, which is a function of the slow time $T = \epsilon^2 t$. We fit these trajectories to Eq. (9) in the main text with \mathcal{F} as the fitting parameter in order to obtain the simulation points of Fig. 4 of the main text. This was done in two ways: i) Taking a derivative with respect to time of the time-averaged trajectories from simulations, one obtains \mathcal{F} directly from Eq. (9) of the main text. ii) The explicit analytical solution to Eq. (9) of the main text, namely, $r_p(T) = (r_p(0) - 48\alpha^2 T \lambda \mathcal{F})^{1/8}$, was fitted to the time-averaged trajectories from DNS using the method of least squares over a time interval that excludes the period of initial transient behavior in simulations. We found that both these strategies yielded virtually identical values for \mathcal{F} , which are displayed in Fig.4 of the main text.

5. Simulation methods and details

In order to perform three dimensional flow–structure interaction simulations with deforming geometries, we use the remeshed Vortex Method (rVM) described in (11). Here, we list our simulation methodology and parameters for completeness and reproducibility, as well as convergence tests used to assess simulations accuracy.

A. Fluid-structure interaction. We briefly recap the governing equations and numerical method used for our simulation. We consider incompressible viscous flows in an unbounded domain in which two density-matched spherical bodies (i.e. bubble and particle) are immersed. We denote the computational domain as $\Omega = \Omega_f \cup \Omega_B$, where Ω_f is the fluid domain and $\Omega_B = \Omega_b \cup \Omega_p$ is the domain in which the bubble (Ω_b) and particle (Ω_p) reside, and denote the interface between the fluid and the bodies as $\partial \Omega_B$. Both the bubble and the particle are then represented by mollified characteristic functions $\chi_b(\mathbf{x})$ and $\chi_p(\mathbf{x})$, respectively, on a regular Cartesian grid mesh such that $\chi_b(\mathbf{x}) = 1$ for $\mathbf{x} \in \Omega_b$, $\chi_p(\mathbf{x}) = 1$ for $\mathbf{x} \in \Omega_p$, and $\chi_b(\mathbf{x}) = \chi_p(\mathbf{x}) = 0$ for $\mathbf{x} \in \Omega_f$. In order to avoid discontinuities, for each of the bodies, we smoothly blend the χ values using the mollification function

$$\chi(d) = \begin{cases}
0 & d < -\epsilon_{\rm m}, \\
\frac{1}{2} \left(1 + \frac{d}{\epsilon_{\rm m}} + \frac{1}{\pi} \sin(\pi \frac{d}{\epsilon_{\rm m}})\right) & |d| \le \epsilon_{\rm m}, \\
1 & d > \epsilon_{\rm m},
\end{cases}$$
[28]

where d is the signed-distance to the body–fluid interface, and $\epsilon_{\rm m}$ is a user-defined smoothing parameter. We then solve the incompressible Navier–Stokes equation eq. (29) in its velocity–vorticity form

$$\nabla \cdot \mathbf{u} = 0, \quad \frac{D\omega}{Dt} = (\omega \cdot \nabla)\mathbf{u} + \nu \nabla^2 \omega + \lambda_{\text{penal}} \nabla \times (\chi(\mathbf{u}_{\text{B}} - \mathbf{u})) \quad \mathbf{x} \in \Omega$$
 [29]

where ω is the vorticity field, \mathbf{u} is the fluid velocity field, \mathbf{u}_B is the body velocity and ν is the kinematic viscosity. Here $\lambda_{\text{penal}} \gg 1$ is the penalization parameter and $\lambda_{\text{penal}} \nabla \times (\chi(\mathbf{u}_B - \mathbf{u}))$ is the Brinkmann penalization term used to approximate the no-slip boundary condition (11). We note that while a bubble interface is a no-stress boundary condition instead of no-slip, in case of a bubble oscillating in pure breathing mode, where tangential boundary conditions have no effect, the same irrotational flow response results for an isolated bubble. The interface gradients of the mollification layer can, however, induce low levels of spurious vorticity, which are explicitly removed from the fluid in our solver by smoothly blending the vorticity to zero on the interface using a characteristic function analogous to (28). This ensures a consistent, streaming-free flow field and in addition reduces coupling effects between the disturbance flow and the bubble interface, in line with the theoretical treatment.

In using this method, fluid velocity within a body is forced to approach the body velocity (i.e. $\mathbf{u}(\mathbf{x}) = \mathbf{u}_{\mathrm{B}}(\mathbf{x})$ for $\mathbf{x} \in \Omega_{\mathrm{B}}$). The body velocity \mathbf{u}_{B} can be decomposed into its rigid components of motion and the body deformation velocity field as $\mathbf{u}_{\mathrm{B}}(\mathbf{x},t) = \mathbf{u}_{\mathrm{T}}(t) + \mathbf{u}_{\mathrm{R}}(\mathbf{x},t) + \mathbf{u}_{\mathrm{def}}(\mathbf{x},t)$, where \mathbf{u}_{T} and \mathbf{u}_{R} are rigid translational and rotational velocities, and $\mathbf{u}_{\mathrm{def}}$ is the (imposed) deformation velocity field. The body rigid velocity (as a result of action from the fluid) is obtained via a projection approach (11) where \mathbf{u}_{T} and \mathbf{u}_{R} are computed through the conservation of momentum in the system. The imposed deformation velocity field used to prescribe the bubble's breathing mode is $\mathbf{u}_{\mathrm{def}}(\mathbf{x},t) = \frac{\mathbf{x}}{r_b(t)} \epsilon a_b \omega \sin(\omega t)$ for $\mathbf{x} \in \Omega_{\mathrm{B}}$, where $r_b(t)$ is the instantaneous bubble radius. This methodology based on remeshed vortex methods, penalization and projection has been validated across a range of fluid–structure interaction problems involving both rigid and deformable bodies, from bluff body flows to biological swimming (11–15). Recently, it has also been demonstrated in resolving the spatio-temporal scales related to oscillatory flow problems, particularly in viscous streaming settings involving individual and multiple arbitrary-shaped bodies, both in two and three dimensions (16, 17). For a more detailed description of the numerical method, we refer to (11).

B. Simulation details. We simulate both the bubble and the particle as spheres of radii $a_b = 0.01$ and $a_p = 0.002$, respectively (so that $a_p/a_b = 0.2$), and set the mollification smoothing parameter $\epsilon_{\rm m} = \sqrt{2}\Delta x$ used in the characteristic function eq. (28), where Δx is the simulation grid size. The computational domain is initialized with a physical size of [-2, 5.875] $a_b \times [-1.9125, 1.9125]$ $a_b \times [-1.912$

prescribing $\mathbf{u}_{\mathrm{def}}(\mathbf{x},t) = \frac{\mathbf{x}}{r_b(t)} \epsilon a_b \omega \sin(\omega t)$ for $\mathbf{x} \in \Omega_{\mathrm{B}}$, so that the interface of the bubble moves with radial velocity $\epsilon a_b \omega \sin(\omega t)$. Throughout this paper, we set $\epsilon = 0.05$ and $\omega = 16\pi$. The viscosity ν is set based on $\lambda = a_p^2 \omega/(3\nu)$ and the simulation is allowed to run until the particle's steady velocity is achieved (typically 40–200 oscillation cycles, depending on λ where larger λ require longer time for transient effects to vanish). Finally, we note that the bubble, particle and fluid are density-matched and density is set to unity.

- **C.** Implementation and resources. The simulation algorithm is implemented in Fortan90 and relies on MPI for distributed memory parallelism. The software relies on Parallel Particle Mesh library (PPM) (18) which provides a convenient abstraction layer over MPI particle—mesh operations, mapping on processors, processor communication and load-balancing. The software also uses FFTW3 library for Poisson solves and HDF library for data output, visualization and post-processing. The simulations performed in this paper typically run for 48–96 hours on 16 nodes, each with 64 threads, on the Stampede2 supercomputing facility.
- **D. Resolution convergence test.** It is important that we capture the different length scales involved in order to properly resolve the physics at play. We first identify the different physical (bubble oscillations ϵa_b , particle oscillations, Stokes boundary layer thickness δ_S) and numerical (mollification length $\epsilon_{\rm m} = \sqrt{2}\Delta x$) length scales in this problem. Taking these scales into consideration, we then need to ensure that (i) the oscillations are properly resolved (i.e. $\Delta x <$ oscillation amplitudes) and (ii) δ_S measured from the bubble interface is not embedded in or under-resolved relative to the mollification region (i.e. $\delta_S > \epsilon_{\rm m}$).

We conduct a resolution convergence test where we run a series of separate simulations with increasing resolution (hence decreasing Δx). We then track the particle's trajectory (via center-to-center distance between bubble and particle) and observe a convergence towards a fixed trajectory, beyond which decreasing the grid size further does not significantly affect the results while requiring considerably larger computational cost. We illustrate the convergence behavior in Figure S2 for the case of $r_p(0) = 2$ and $\lambda = 20$, deliberately chosen from the larger λ regime in the test cases explored in this paper so that δ_S is thin (hence requiring finer Δx to resolve). Here we note that a grid size of $\Delta x = 1.40625 \times 10^{-2} \ a_b$ provides a good compromise between computational cost and accuracy as it resolves the physical and numerical length scales reasonably well, effectively ensuring (i) Δx is finer than oscillation amplitudes and (ii) $\delta_S > \epsilon_{\rm m}$. Therefore, throughout this paper, we use $\Delta x = 1.40625 \times 10^{-2} \ a_b$ for all our simulations.

E. Domain size convergence test. In order to perform the simulations within feasible computational costs while ensuring that all the length scales involved are properly resolved (see section D), we adjust our simulation domain to a reasonable size such that effects from domain boundaries do not affect the computed results. We perform a simple test by fixing $\Delta x = 2.8125 \times 10^{-2} \ a_b$ and explore the boundary effects for different domain sizes. The case of study here is $r_p(0) = 2$ and $\lambda = 1$ (hence a thick δ_S that might interact with domain boundaries). We note that while a lower resolution is used here for exploration (see section D), the δ_S is still resolved in the simulations (i.e. $\delta_S > \epsilon_{\rm m}$) and the test still serves to demonstrate the effects from domain boundaries. Figure S3 shows the time-averaged trajectories for different domain sizes 0.375 L, 0.5 L and L, where L = [-4,11.75] $a_b \times [-3.825,3.825]$ $a_b \times [-3.825,3.825]$ $a_b \times [-3.825,3.825]$ $a_b \times [-3.825,1.9125]$ $a_b \times [-1.9125,1.9125]$ $a_b \times [-1.9125,1.9125]$

6. Comparison with experimental data

The trajectory plotted in Fig. 1(b) of the main text was obtained directly from our own experiments by tracking a neutrally buoyant particle of radius $10\mu m$ transported past an oscillating cylindrical bubble. The particle experiences an attractive force towards the bubble leading to a sizeable displacement across fluid streamlines (towards the bottom channel wall) that is a substantial fraction of the particle size. This observation is in direct contradiction to existing theories like acoustic radiation forces (19–30), which depend crucially on contrasts of density or compressibility between the particle and its surrounding fluid and, thus, predict no attraction at all or a much too weak effect.

We have refrained from presenting a direct comparison to theory in the main text, because a rigorous modeling on a par with the formalism we present requires additional elements: (a) the background flow field in experiment is a superposition of a channel transport flow and a flow field resulting from a complicated bubble oscillation combining volume and shape modes (cf. (31)), whose amplitudes and phases are not easy to measure with great accuracy; (b) by nature of this background flow, the particle's trajectory approaches the bubble quite closely, necessitating the incorporation of boundary effects, i.e., taking into account the location of the bubble surface as a fluid boundary.

Our reciprocal-theorem-based approach can, in principle, be generalized to any time-dependent background flow as well as adapted to include the effect of (channel) walls and/or boundaries (as detailed in Sec. 1). However, providing a theory prediction for this experimental case to the same degree of systematic detail as the current manuscript would lead to a much more technical formalism, obscuring the newly derived inertial force in its closed form.

Nonetheless, we can attempt an approximate modeling combining the flow field approximation of (31), the lubrication repulsion of (32, 33) (the leading boundary effect), and the force computation of the present manuscript (i.e., modeling the radial component of inertial force as dominant over any tangential force component present in the experimental flow). While the resulting trajectory does not show point-by-point agreement with experiment, the eventual particle displacement, perhaps the most relevant quantity here, is of very similar magnitude (3.4 μ m compared to the experimental 2.8 μ m). Conversely,

a computation without the attractive inertial force results in no displacement at all (Fig. S4). We caution that while this agreement is encouraging, because of the approximations it should not be taken as a quantitative test of the rigorous derivation and elucidation of the inertial force in the main paper. Future work will carefully incorporate the additional effects of flow field complexity and boundaries, further generalizing the theory in a systematic way.

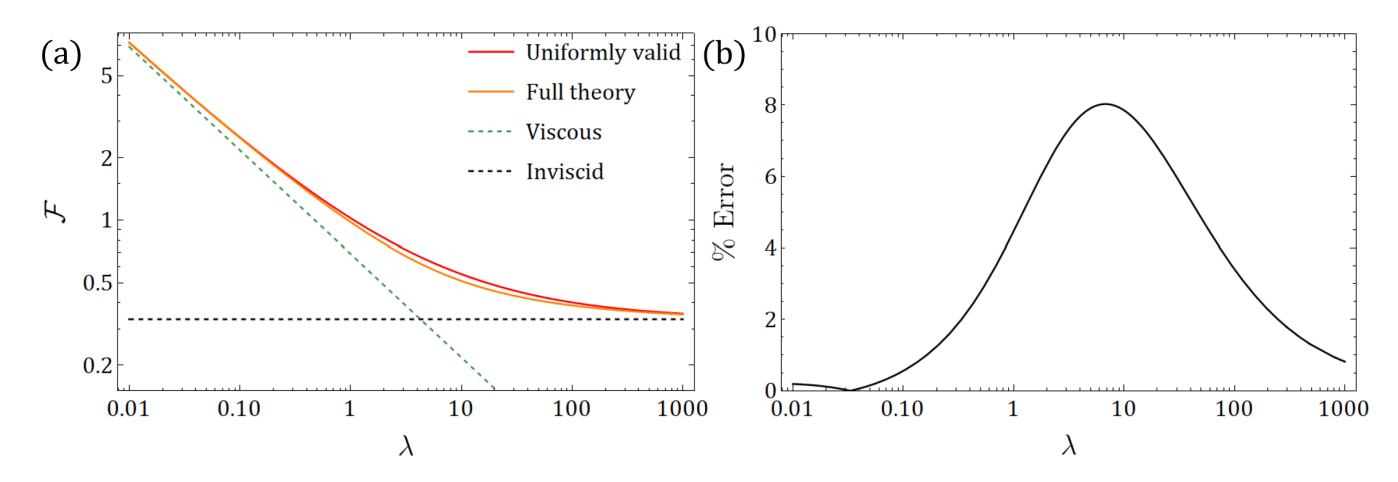


Fig. S1. (a) Logarithmic plot of the overall inertial force magnitude $\mathcal{F}(\lambda)$: the uniformly valid expression (red) closely tracks the full solution (orange) while the inviscid theory (gray dashed) severely underestimates the inertial force even for moderately large λ . (b) The magnitude of the percentage error between the uniformly valid and full solutions is small throughout the entire range of λ , with a maximum error of $\sim 8\%$ where the two limits blend, as one would expect.

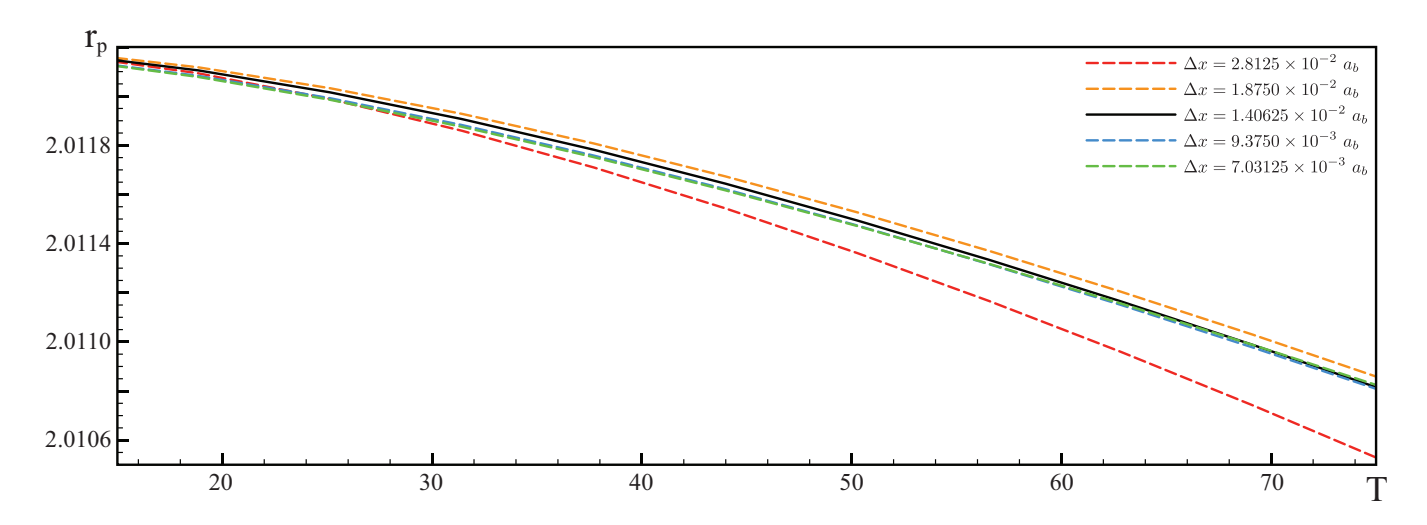


Fig. S2. Resolution convergence: Trajectory of particle for simulations with different Δx for the case of $r_p(0)=2$ and $\lambda=20$.

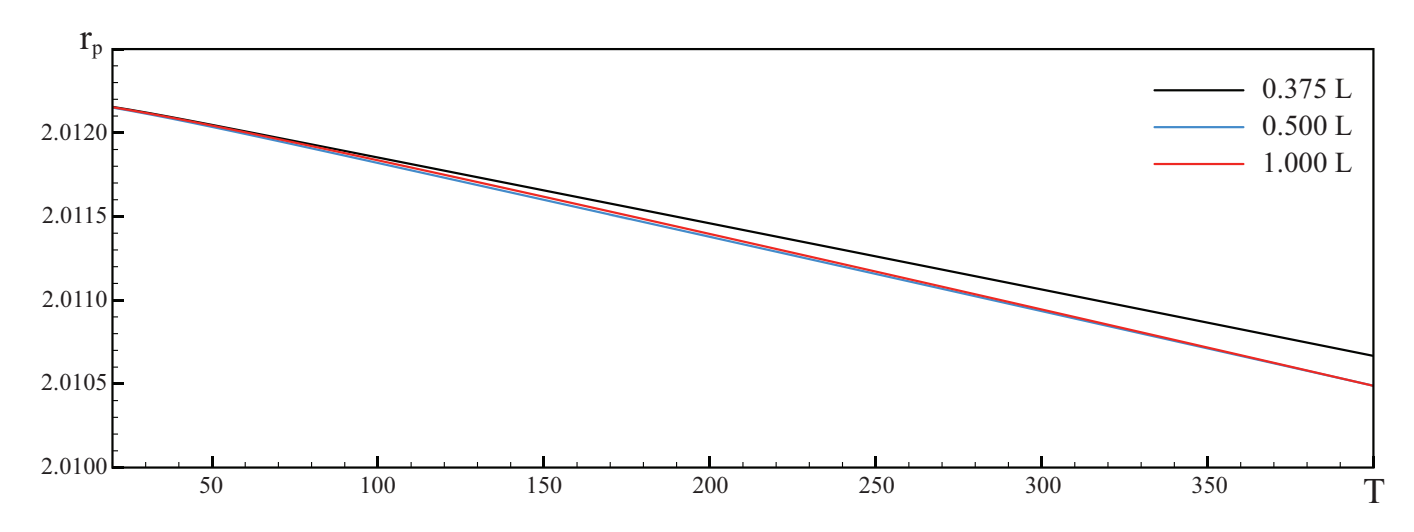


Fig. S3. Domain convergence: Trajectory of particle for simulations with different domain size for the case of $r_p(0)=2$ and $\lambda=1$.

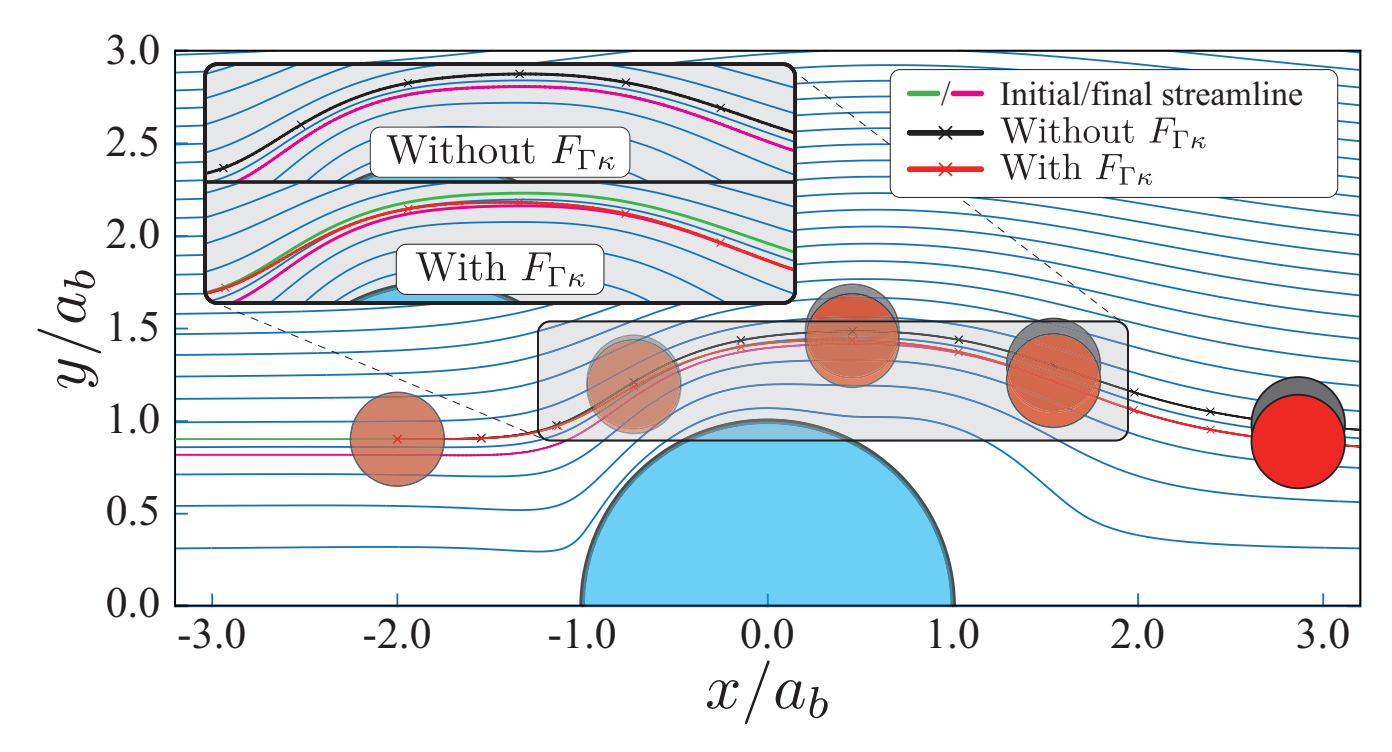


Fig. S4. A particle trajectory computed using the current uniformly valid theory for radial inertial force combined with the streaming and transport flow fields around a cylindrical bubble shows a displacement downwards (attraction to the bubble, inset) consistent with the experimental observation of Fig.1b of the manuscript (red line and red symbols). A computation without the newly introduced inertial force yields no significant displacement (black line and gray symbols). The parameters reflect those of the experiment in Fig.1b, and the final displacement of the particle where it leaves the field of view is $3.4\mu m$, close to the mean of $2.8\mu m$ observed in experiment.

References

- 1. MR Maxey, JJ Riley, Equation of motion for a small rigid sphere in a nonuniform flow. *The Phys. Fluids* **26**, 883–889 (1983).
- 2. R Cox, H Brenner, The lateral migration of solid particles in poiseuille flow—i theory. Chem. Eng. Sci. 23, 147–173 (1968).
- 3. B Ho, L Leal, Inertial migration of rigid spheres in two-dimensional unidirectional flows. J. fluid mechanics 65, 365–400 (1974).
- 4. K Hood, S Lee, M Roper, Inertial migration of a rigid sphere in three-dimensional poiseuille flow. J. Fluid Mech. 765, 452–479 (2015).
- 5. LD Landau, E Lifshitz, Course of Theoretical Physics Vol. 6 Fluid Mechanies. (Pergamon Press), (1959).
- C Pozrikidis, , et al., Boundary integral and singularity methods for linearized viscous flow. (Cambridge University Press), (1992).
- 7. PM Lovalenti, JF Brady, The hydrodynamic force on a rigid particle undergoing arbitrary time-dependent motion at small reynolds number. J. Fluid Mech. 256, 561–605 (1993).
- 8. H Stone, J Brady, P Lovalenti, Inertial effects on the rheology of suspensions and on the motion of individual particles. preprint (2001).
- 9. B Rallabandi, Inertial forces in the maxey-riley equation in nonuniform flows. Phys. Rev. Fluids 6, L012302 (2021).
- 10. S Danilov, M Mironov, Mean force on a small sphere in a sound field in a viscous fluid. *The J. Acoust. Soc. Am.* **107**, 143–153 (2000).
- 11. M Gazzola, P Chatelain, WM Van Rees, P Koumoutsakos, Simulations of single and multiple swimmers with non-divergence free deforming geometries. *J. Comput. Phys.* **230**, 7093–7114 (2011).
- 12. M Gazzola, C Mimeau, AA Tchieu, P Koumoutsakos, Flow mediated interactions between two cylinders at finite re numbers. *Phys. fluids* **24**, 043103 (2012).
- 13. M Gazzola, WM Van Rees, P Koumoutsakos, C-start: optimal start of larval fish. J. Fluid Mech. 698, 5-18 (2012).
- 14. M Gazzola, B Hejazialhosseini, P Koumoutsakos, Reinforcement learning and wavelet adapted vortex methods for simulations of self-propelled swimmers. SIAM J. on Sci. Comput. 36, B622–B639 (2014).
- 15. M Gazzola, AA Tchieu, D Alexeev, A de Brauer, P Koumoutsakos, Learning to school in the presence of hydrodynamic interactions. *J. Fluid Mech.* **789**, 726–749 (2016).
- 16. T Parthasarathy, FK Chan, M Gazzola, Streaming-enhanced flow-mediated transport. J. Fluid Mech. 878, 647–662 (2019).
- 17. Y Bhosale, T Parthasarathy, M Gazzola, Shape curvature effects in viscous streaming. J. Fluid Mech. 898, A13 (2020).
- 18. IF Sbalzarini, et al., Ppm–a highly efficient parallel particle–mesh library for the simulation of continuum systems. *J. Comput. Phys.* **215**, 566–588 (2006).
- D Di Carlo, D Irimia, RG Tompkins, M Toner, Continuous inertial focusing, ordering, and separation of particles in microchannels. PNAS 104, 18892–18897 (2007).
- ME Warkiani, et al., Malaria detection using inertial microfluidics. Lab on a Chip 15, 1101-1109 (2015).
- 21. P Rogers, A Neild, Selective particle trapping using an oscillating microbubble. Lab on a Chip 11, 3710-3715 (2011).
- 22. A Hashmi, G Yu, M Reilly-Collette, G Heiman, J Xu, Oscillating bubbles: a versatile tool for lab on a chip applications. Lab on a Chip 12, 4216–4227 (2012).
- 23. Y Chen, S Lee, Manipulation of biological objects using acoustic bubbles: a review. *Integr. comparative biology* **54**, 959–968 (2014).
- 24. Y Chen, et al., Onset of particle trapping and release via acoustic bubbles. Lab on a Chip 16, 3024–3032 (2016).
- 25. IS Park, JH Shin, YR Lee, SK Chung, On-chip micromanipulation using a magnetically driven micromanipulator with an acoustically oscillating bubble. Sensors Actuators A: Phys. 248, 214–222 (2016).
- 26. V Bjerknes, Fields of force. (General Books), (1906).
- 27. TA Hay, MF Hamilton, YA Ilinskii, EA Zabolotskaya, Model of coupled pulsation and translation of a gas bubble and rigid particle. *The J. Acoust. Soc. Am.* **125**, 1331–1339 (2009).
- 28. WT Coakley, W Nyborg, Cavitation; dynamics of gas bubbles; applications. *Ultrasound: Its applications medicine biology* 3, 77–159 (1978).
- 29. H Bruus, Acoustofluidics 7: The acoustic radiation force on small particles. Lab on a Chip 12, 1014–1021 (2012).
- 30. L Schmid, DA Weitz, T Franke, Sorting drops and cells with acoustics: acoustic microfluidic fluorescence-activated cell sorter. *Lab on a Chip* **14**, 3710–3718 (2014).
- 31. B Rallabandi, C Wang, S Hilgenfeldt, Two-dimensional streaming flows driven by sessile semicylindrical microbubbles. *J. Fluid Mech.* **739**, 57–71 (2014).
- 32. R Thameem, B Rallabandi, S Hilgenfeldt, Fast inertial particle manipulation in oscillating flows. *Phys. Rev. Fluids* 2, 052001 (2017).
- 33. S Agarwal, B Rallabandi, S Hilgenfeldt, Inertial forces for particle manipulation near oscillating interfaces. *Phys. Rev. Fluids* 3, 104201 (2018).